iScience

Article

Effects of corticothalamic feedback depend on visual responsiveness and stimulus type

Graphical abstract

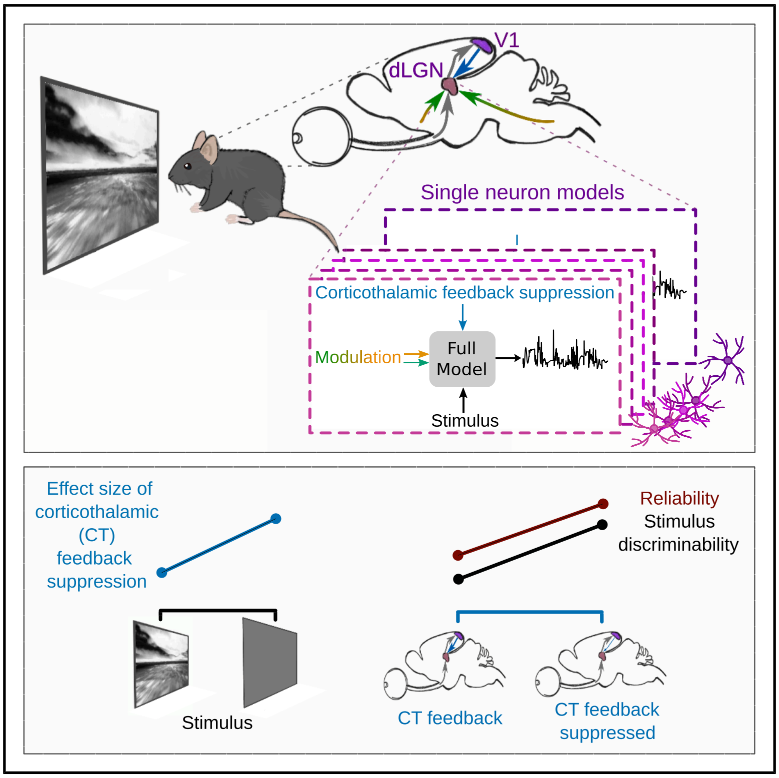

Authors

Lisa Schmors, Ann H. Kotkat,
Yannik Bauer, ..., Sacha Sokoloski,
Philipp Berens, Laura Busse

Correspondence

philipp.berens@uni-tuebingen.de (P.B.),
busse@bio.lmu.de (L.B.)

In brief

Neuroscience; Sensory neuroscience

Highlights

- dLGN activity is influenced by behavioral state and corticothalamic (CT) feedback
- This influence is most prominent for dLGN neurons with poor visual responsiveness
- CT feedback is strongest in the absence of a patterned stimulus
- CT feedback suppression can improve stimulus decoding

Schmors et al., 2025, iScience *28*, 112481
June 20, 2025 © 2025 The Authors. Published by Elsevier Inc.
https://doi.org/10.1016/j.isci.2025.112481

iScience

CellPress
OPEN ACCESS

Article

Effects of corticothalamic feedback depend on visual responsiveness and stimulus type

Lisa Schmors,[1,6] Ann H. Kotkat,[3,4,6] Yannik Bauer,[3,4,6] Ziwei Huang,[1,2] Davide Crombie,[3,4]
Lukas Sebastian Meyerolbersleben,[3,4] Sacha Sokoloski,[1] Philipp Berens,[1,2,7,*] and Laura Busse[3,5,7,8,*]
[1]Hertie Institute for AI in Brain Health, University of Tübingen, 72076 Tübingen, Germany
[2]Tübingen AI Center, University of Tübingen, 72076 Tübingen, Germany
[3]Division of Neurobiology, Faculty of Biology, LMU Munich, 82152 Planegg-Martinsried, Germany
[4]Graduate School of Systemic Neurosciences (GSN), LMU Munich, 82152 Planegg-Martinsried, Germany
[5]Bernstein Center for Computational Neuroscience, 82152 Planegg-Martinsried, Germany
[6]These authors contributed equally
[7]Senior author
[8]Lead contact
*Correspondence: philipp.berens@uni-tuebingen.de (P.B.), busse@bio.lmu.de (L.B.)
https://doi.org/10.1016/j.isci.2025.112481

SUMMARY

In the dorsolateral geniculate nucleus (dLGN) of the thalamus, stimulus-driven signals combine with modulatory inputs such as corticothalamic (CT) feedback and behavioral state, but their impact in shaping dLGN activity is debated. We recorded extracellular responses in the dLGN of mice viewing a movie stimulus, while photosuppressing CT feedback and tracking locomotion and pupil size. Using generalized linear models fit to single neuron responses, we found that including CT feedback and behavioral state improved model predictions, especially for a subpopulation of neurons poorly responsive to the movie. Intriguingly, the impact of CT feedback was stronger without a patterned visual stimulus. Finally, for neurons sensitive to CT feedback, visual stimuli could be more easily discriminated when CT feedback was suppressed. Together, these results show that the effects of modulatory inputs in dLGN depend on visual responsiveness and stimulus type, with CT feedback affecting sensitivity and reliability, potentially to tune the thalamic relay.

INTRODUCTION

Visual information is processed through a hierarchy of brain areas, which are connected by feedforward and feedback projections. Early in this hierarchy is the dorsolateral geniculate nucleus (dLGN) of the thalamus, a central node for visual information *en route* from the retina to the primary visual cortex (V1).[1,2] The dLGN has long been recognized as one of the first visual stages that combines stimulus-driven inputs with additional modulatory inputs,[3] such as signals arising from L6 corticothalamic (CT) feedback,[4–8] and signals from the brainstem carrying information related to behavioral state[9–12] and arousal.[3,10,13,14] How visually driven and modulatory inputs are quantitatively combined to yield dLGN responses, potentially in a cell-type and stimulus dependent way, remains poorly understood.

On the one hand, it has been firmly established that, even during wakefulness, dLGN responses are modulated according to the animal's internal[9,15] and overt behavioral state.[15–17] For instance, in the mouse, locomotion-[11,18] or pupil-indexed arousal[9,10,13,14,19] are associated with overall enhancements of firing rates in dLGN, which seem to preferentially affect specific neuronal populations depending on their spatiotemporal feature selectivity.[18,19] Similar to related findings in the somatosensory system,[20] the increase in dLGN firing rates seems to be a necessary condition for the sustained depolarization of primary visual cortex during active behaviors.[9]

On the other hand, little consensus has been achieved for dLGN modulations by CT feedback, where a plethora of previous studies have together highlighted its diverse and potentially stimulus-dependent effects. For instance, CT feedback is known to sharpen spatial dLGN RFs and increase contextual effects,[6,7,21–24] by enhancing or suppressing dLGN firing rates depending on grating size and potentially its spatial homogeneity or contrast. The sign of CT feedback effects might further depend on the alignment of retinotopic position and/or feature selectivity between L6 and dLGN neurons.[6,7,25] The combination of enhancing and suppressing effects of CT feedback are likely mediated by a differential engagement of both direct excitatory and indirect inhibitory pathways, whose balance will depend on the stimulus selectivity, connectivity and intrinsic properties of corticothalamic neurons in L6 of V1, neurons in the thalamic reticular nucleus (TRN) and dLGN.[8,26] Indeed, a landmark study in the somatosensory corticothalamic system[26] has demonstrated that differential short-term synaptic plasticity rules in the direct corticothalamic pathway and the indirect pathway through the TRN can change the sign of corticothalamic influence depending on cortical L6 firing frequency.

Generalized linear models (GLMs) provide an established framework for statistical analysis of neural responses, which can help to disentangle the combined impact of multiple stimulus-driven and modulatory influences and investigate their properties.[27–29] While GLMs are relatively simple phenomenological models, they offer the advantage of being interpretable: for instance, GLM kernels learned for the visual stimulus approximate the integration by the spatiotemporal receptive field (RF), and kernels learned for any additional inputs represent spike-induced gain adjustments.[28,30] First applied in the retina,[28,31] GLMs have since then been used in numerous studies to separate influences of the visual stimulus and other variables, such as spike history, interneuronal interaction effects, task-engagement, learning, reward prediction, task-related motor action, locomotion, and arousal.[32–38] One recent extension of classical GLMs is to estimate RFs by choosing a set of cubic spline basis functions in order to encode smoothness, decrease the number of parameters, and thus be more data efficient.[39]

Here, we investigated how feedforward, stimulus-driven signals, feedback signals, and behavioral state jointly influence dLGN activity in awake, head-fixed mice viewing a rich movie stimulus. We simultaneously recorded extracellular dLGN activity, mouse run speed and pupil size, while photosuppressing CT feedback. We then fitted a spline-GLM model containing kernels for the spatiotemporal RF, CT feedback, and behavior to predict responses of dLGN neurons. The learned kernels were biologically plausible, including diverse spatiotemporal RFs, as well as kernels for behavior and CT feedback. Including modulatory inputs overall improved the prediction of dLGN responses; the improvements, however, were most prominent for a subpopulation of neurons that were poorly predicted by the movie stimulus. Focusing on the effects of CT feedback, we found that these effects depended on stimulus type in both the model and the data, being stronger, more prevalent and faster during the absence of a patterned visual stimulus. Using the spline-GLM for *in silico* experiments and confirming its predictions *in vivo*, we demonstrate, for CT feedback-sensitive, individual dLGN neurons, that stimulus discrimination during CT feedback suppression was enhanced. We relate our findings to previous frameworks about CT feedback, injecting synaptic background noise to enhance sensitivity and linearity of dLGN responses.[40,41] We conclude that the effects of modulatory inputs in dLGN can be complex and depend on visual responsiveness and stimulus type, with CT feedback affecting sensitivity and reliability, potentially to tune the thalamic relay.

RESULTS

Dorsolateral geniculate nucleus responses to movies are modulated by behavioral variables and corticothalamic feedback suppression

To investigate how CT feedback, locomotion and arousal modulate thalamic responses, we recorded *in vivo* extracellular dLGN activity in response to a rich movie stimulus in four head-fixed mice together with running speed and pupil size, while randomly photo-suppressing CT feedback (Figure 1A). For the photo-suppression of CT feedback, we conditionally expressed the soma-targeting, chloride-conducting channelrhodopsin stGtACR2-RFP[42] in L6 CT pyramidal cells, by injecting a small volume of Cre-dependent AAV into V1 of Ntsr1-Cre mice.[43] The localization of stGtACR2 to L6 CT somata and the accurate placement of electrodes were confirmed through *postmortem* histological analyses (Figure 1B). During electrophysiological recordings, the mouse viewed a rich movie stimulus that consisted of a sequence of black-and-white clips from various feature films ("movies," Figure 1C, top). Here, photo-suppression occurred every second with 50% probability. We also measured the mouse's run speed and pupil size to infer the animal's changing behavioral state.

To develop initial insights into the modulations of dLGN responses by CT feedback and the behavioral inputs, we aligned movie responses to onsets of photo-suppression, running, and pupil dilation. We found that certain neurons responded to the onset of CT feedback suppression with a substantial reduction in firing rate (Figures 1D–1F, left, OFF-ON transitions in *blue*), while others showed milder effects or no modulation at all (Figure 1F, left). Despite the relatively small effect size, the overall reduction of dLGN firing rates during CT feedback suppression was genuine, as none of the recorded neurons in a control mouse without opsin expression showed systematic modulations at light onset (Figures S1A and S1B). Furthermore, neural responses aligned to time points in which the optogenetic light was not switched on (i.e., OFF-OFF transitions in *gray*, Figures 1D and 1E) did not show any systematic modulation (Figure S1C). Finally, neurons with stronger CT feedback effects were closer to each other (Figure S2), as predicted by the topography of the corticothalamic system.[7,44–46] Consistent with previous findings,[10,11,18,47] we also found that firing rates could gradually increase around transitions from sitting to running (Figure S3A), and during pupil dilation (Figure S3B).

These modulations of dLGN responses were also observed across the population of recorded neurons. Specifically, dLGN firing rates during the time of CT feedback suppression compared to periods without CT feedback suppression were reduced (*control* vs. *CT FB supp.* mean: 12.6 vs. 11.5 Hz, $p = 1.24 \times 10^{-2}$, paired Wilcoxon signed-rank test; Figure 1F, left), while time windows with running and dilated pupil were associated with an overall increase in average firing rates (*sit* vs. *run* mean: 11.0 vs. 12.8 Hz, $p = 8.31 \times 10^{-16}$, Figure 1F, middle; *small* vs. *large pupil* mean: 11.0 vs. 13.0 Hz, $p = 4.98 \times 10^{-7}$, paired Wilcoxon signed-rank test; Figure 1F, right). Although these modulations affected the recorded dLGN population on average, we also noticed considerable neuron-to-neuron variability. Indeed, for all three modulatory inputs, we found neurons that were affected to various degree across the different conditions (Figure 1F, insets).

So far, we have shown that dLGN responses to our movie stimulus were modulated by multiple additional inputs; this simple analysis on the mean firing rates, however, did not take into account potential correlations between the different inputs. Consistent with various previous studies,[9,48,49] we found a positive correlation between pupil diameter and running speed ($r = 0.18 \pm 0.17$, mean ± SD; $p < 0.001$ for 7/10 experiments, permutation test; Figure S3C). Moreover, we found pupil size to also be influenced by stimulus brightness, where lower average intensity of movie frames was associated with larger pupil

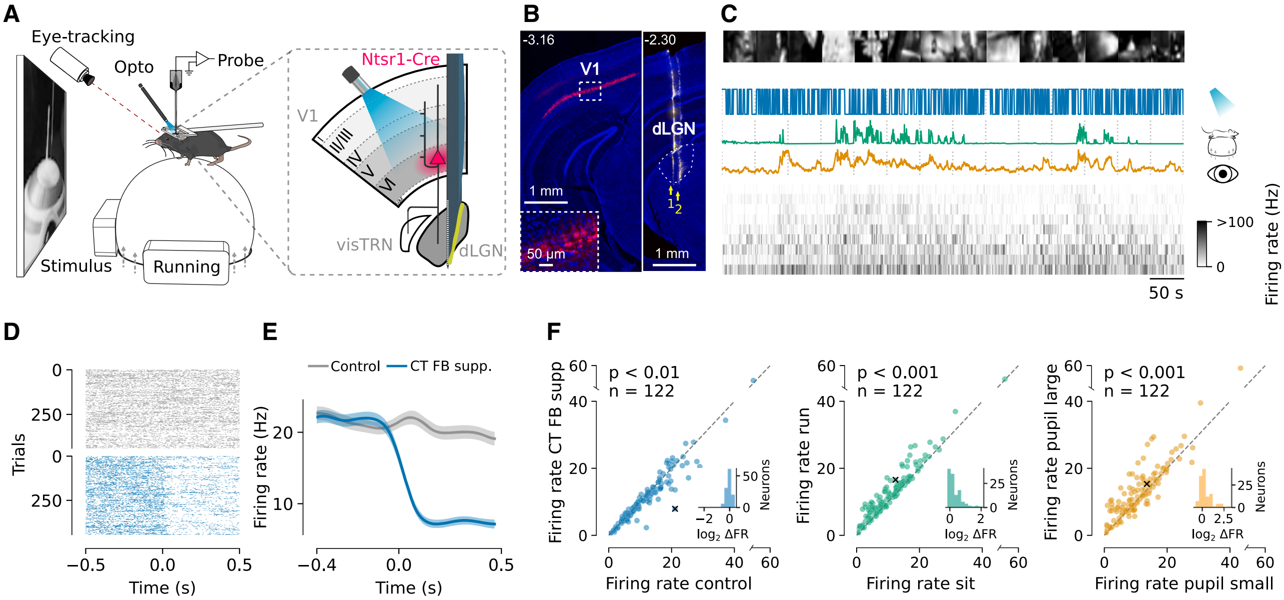

Figure 1. CT feedback and behavior modulate dLGN responses to movies

(A) Schematic of the recording setup and photo-suppression of V1 L6 CT pyramidal neurons in Ntsr1-Cre mice with Cre-dependent AAV-stGtACR2-RFP.

(B) Histology. *Left:* Coronal section near the V1 injection site, with stGtACR2-RFP expression (*red*) in Ntsr1+ somata. *Blue:* DAPI; scale bar: 1 mm. *Inset:* Magnification of area marked by dotted rectangle. Scale bar: 50 μm. *Right:* Coronal section of dLGN recording sites, with electrode tracks for two consecutive recording sessions (arrows 1 and 2) marked with DiI (*yellow*). Scale bar: 1 mm. *Dotted line*: dLGN contour. *Numbers on top*: position relative to Bregma in mm.

(C) Snippet of an example dLGN recording. *Top to bottom*: example frames of the movie stimulus, photo-suppression pulse train (*blue*), running speed (*green*), pupil area (*yellow*), and time varying firing rate (sorted by first principal component) of simultaneously recorded dLGN neurons.

(D) Raster plot of responses of an example dLGN neuron, time locked to the onset of CT feedback photo-suppression (*blue*, OFF-ON transition) and to control periods without photosuppression (*gray*, OFF-OFF transition). Note that the example neuron illustrates the observed effect of CT feedback photo-suppression, but the size of the effect is not representative of that observed in the population of recorded dLGN neurons.

(E) Corresponding PSTHs (*solid line*: average across trials, *shaded area*: standard error of the mean).

(F) Effects of CT feedback photo-suppression (*left*), locomotion (*middle*), and pupil size (*right*) on dLGN mean firing rates. Example neuron from (D, E) marked with ×. *p* values denote results of a Wilcoxon signed-rank test, $n = 122$ neurons. *Insets:* Histogram of firing rate fold-change relative to control (Δ FR $\log_2$-ratio).

diameters ($r = -0.41 \pm 0.15$, mean ± SD; $p < 0.001$ for 10/10 experiments, permutation test; Figure S3C). Pupil diameter, in turn, is known to influence responses in the early visual system.[50,51]

A spline-based generalized linear model captures dorsolateral geniculate nucleus spatiotemporal RFs and their modulation by corticothalamic feedback and behavior

To disentangle how the various contributions together shape the responses of dLGN neurons, we used a generalized linear model (GLM)[28] that predicted the neuron's firing rate based on a combination of stimulus-driven and modulatory inputs (running speed, pupil size, and CT feedback suppression; Figure 2). The model consisted of one linear kernel for each input, followed by a softplus function that accounted for response nonlinearities (Figure 2A). The shape of the stimulus kernel captured the neuron's spatiotemporal RF, while the shapes of the modulatory kernels captured modulations of the neuron's firing. We employed a GLM with a spline basis[39] in order to efficiently generate smooth kernels, rather than operating directly on the pixels of the visual stimulus or the discrete time bins of the additional inputs (Figures S6A–S6D). The GLM allowed us to effectively capture the temporal correlations between the inputs (see also above, Figure S3C), and the spatiotemporal correlations in pixel intensities in naturalistic stimuli[52,53] (Figure S4A).

After model fitting (see STAR Methods), we assessed the predictive power of the learned kernel shapes using a session-based permutation test (Figure 2B). To keep the temporal statistics of the time series data intact, we provided the model with input data recorded on a different day (for the model inputs "stimulus," "running," and "pupil size") or with synthetic inputs generated with the same statistics as the original (for the "CT feedback suppression" input). To determine significance of the learned kernels, we compared for each input the actual model performance (Pearson's *r*) against a distribution of model performances with that specific input permuted.

We observed a rich diversity of learned GLM kernels for the dLGN neurons' spatiotemporal RFs, the effects of CT feedback, and the behavioral variables. To begin with, we considered three example neurons (Figure 2C). Of these, the first had a negative spatial and a transient temporal stimulus response kernel, which contributed significantly to the model's performance ($p = 3.51 \times 10^{-2}$, permutation test; Figure 2C$_1$, top, same neuron as in Figures 1D and 1E). In addition, it had a significant negative kernel for CT feedback suppression ($p = 2.67 \times 10^{-4}$, permutation test; Figure 2C$_1$, top). In contrast, the running and pupil size

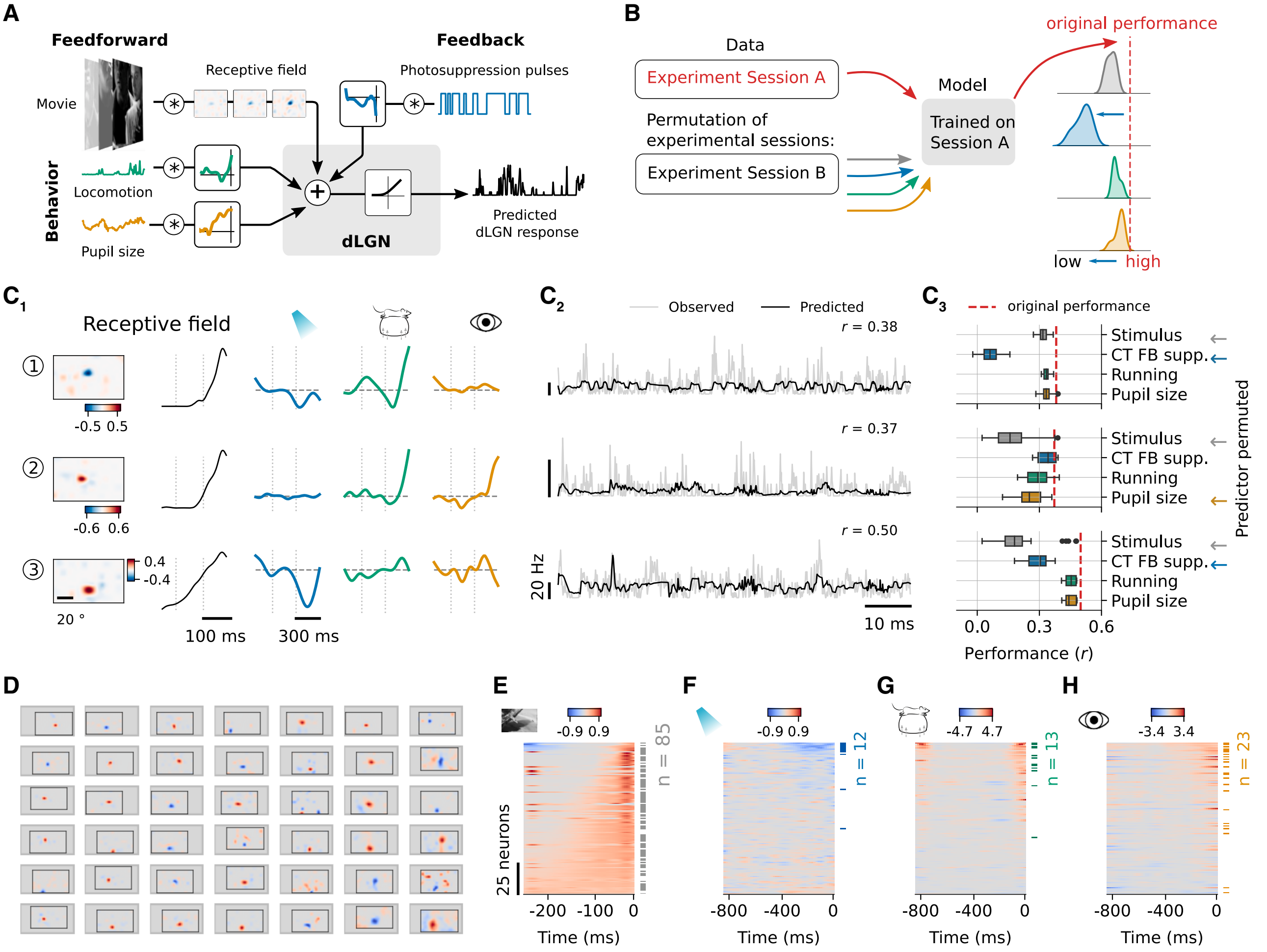

Figure 2. Spline-based GLM captured the RF, the influence of CT feedback, and the impact of behavior on responses of dLGN neurons

(A) Schematics of the spline-GLM model architecture. Firing rate of individual dLGN was predicted as a combination of kernel outputs summed at the linear stage and then passed through a softplus nonlinearity. Each modeled neuron had a kernel for the stimulus and kernels for the three modulatory inputs: run speed (*green*), pupil size (*orange*), and CT feedback suppression (*blue*).

(B) Schematics of the permutation test[54] to assess the significance of the learned kernels. Model performance was evaluated by comparing the actual correlation (Pearson *r*) between predicted and observed firing rates to correlations when one of the inputs was taken from an unrelated experimental session (for movie, running, and pupil size) or randomly generated with the same statistics (for CT feedback suppression). Inputs were considered significant if the actual performance differed from the permuted performance with $p \leq 0.05$.

(C) Three dLGN example neurons, their learned kernels, firing rate predictions, and outcomes of the permutation test (neuron 1 is the same example neuron as in Figures 1D and 1E). (C_1) Spatial and temporal RF components separated by singular value decomposition (SVD, see STAR Methods), along with kernels for the modulatory inputs. (C_2) Observed (*gray*) versus predicted (*black*) firing rates during 80 s of movie presentation. (C_3) Actual model performance (Pearson's *r*, *red dashed line*) and performance for permuted stimulus (*gray*), CT feedback suppression (*blue*), running (*green*), and pupil size (*orange*) inputs. Kernels that contribute significantly to the model's performance are marked with ←. The box displays the quartiles of the distribution, the whiskers represent its range, excluding outliers.

(D) Spatial RFs of example neurons with significant stimulus kernels. *Gray*: outline of common visual space (azimuth: -35–110 deg; elevation: -35–50 deg); *Solid lines*: monitor border.

(E) Temporal RFs (SVD component of the stimulus kernel) in the recorded dLGN population, sorted by their area under the curve.

(F–H) Modulatory kernels in the recorded dLGN population, sorted by their area under the curve, for CT feedback suppression (F), running (G), and pupil size (H). *Horizontal bars, side*: Neurons with significant kernels based on the permutation test. Panels (E–H) show data from all $n = 122$ neurons.

kernels had minimal impact on this neuron's model predictions ($p > 0.05$, permutation test; Figure 2C_1–C_3). The second example neuron exhibited a positive spatial RF with an antagonistic surround ($p = 2.31 \times 10^{-3}$, permutation test; Figure 2C_1, middle). While both behavioral kernels seemed to contribute (Figure 2C_2, middle), only the kernel for pupil size reached significance in the permutation test ($p = 1.13 \times 10^{-2}$). This neuron was also not influenced by CT feedback suppression ($p > 0.05$; Figure 2C_3, middle). Finally, example neuron 3 was primarily visually driven, with a positive RF center and a more sustained temporal response kernel ($p = 2.31 \times 10^{-3}$, permutation test; Figure 2C_1, bottom). It also had a significant negative kernel for

CT feedback suppression ($p = 2.67 \times 10^{-4}$, permutation test; Figure 2C_3, bottom). The other two modulatory kernels had only negligible influences (permutation test, $p > 0.05$; Figure 2C_3, bottom).

The diversity observed in the three example neurons was also evident in the model fits across the population of recorded dLGN neurons, where we obtained a variety of spatiotemporal RFs and combinations of modulatory influences. Assessing the learned spatiotemporal kernels, we found that ~70% of the recorded dLGN neurons were visually responsive to our movie stimulus (85/122 neurons; permutation test visual stimulus, $p \leq 0.05$; Figure S6E). For many of these neurons (representative examples in Figure 2D), the spline-GLM recovered spatial RF properties that were consistent with previous descriptions of mouse dLGN RFs obtained using artificial stimuli[55–57] and in many cases resembled those obtained from conventional sparse noise experiments (Figures S4B and S4C). These properties included various RF locations, RFs with either positive (66%, 56/85 neurons) or negative polarity kernels (34%, 29/85 neurons), a broad range of RF surround strengths (Figures S4D and S4F), and various RF center sizes (Figure S4E). Furthermore, the GLM captured the well-known diversity of temporal response properties of dLGN neurons,[55,58] with some neurons showing more sustained, and others showing more transient temporal kernels (Figures 2E and S4H). Importantly, both the spatial and temporal GLM kernels matched well with the expected polarity and the dynamics obtained from clustering responses into sustained-OFF, Sustained-ON, and Transient groups during full-field luminance steps (Figure S5). This correspondence further underscores our model's capacity to capture meaningful spatiotemporal RF properties and essential visual response characteristics of dLGN neurons based on the recorded movie responses.

We next assessed the learned kernels for the modulatory inputs. According to the permutation test, approximately 10% (12/122 neurons) of the recorded dLGN neurons were affected by CT feedback suppression, 11% (13/122 neurons) by running, and 19% (23/122 neurons) by pupil size (Figures 2F–2H and S6F–S6H). The overall direction of modulation for the significant kernels aligned with the modulation indices obtained directly from the data (Figure 1F): for the significantly modulated neurons, CT feedback suppression kernels were predominantly negative (Figure 2F), while running speed (Figure 2G) and pupil size (Figure 2H) kernels were predominantly positive. These results indicate that both CT feedback and behavioral state variables during the viewing of our natural movie contribute to an overall increase of dLGN responses. Beyond the general sign of modulation, the learned model kernels also offered insights into the temporal dynamics of the modulatory influences: consistent with the well-known slow impact of pupil indexed arousal on responses in the visual system,[48,49] we found that kernels for pupil size had a more sustained profile compared to kernels for running modulations (time to half max kernel running vs. pupil size: 106.3 ms vs. 146.3 ms, Wilcoxon signed-rank test: $p = 7.51 \times 10^{-3}$, Figure S6P). Separating the recorded dLGN neurons by their extracellular waveshape to distinguish broad-spiking, putative relay cells, from narrow-spiking, putative local dLGN interneurons, yielded no significant difference in sensitivity to stimulus or modulatory inputs, likely due to the low number of putative dLGN interneurons in our sample (Figures S6Q–S6T). Taken together, the ability to learn differential kernels and a close correspondence between data-driven modulation indices and the impact of the modulatory inputs for model performance (Figures S7D–S7G) demonstrate that our GLM model was successful in extracting the impact of the various modulatory inputs.

Despite the spline-GLM's overall success in predicting dLGN responses and learning biologically plausible kernels, it also faced challenges. First, it was not successful in capturing fast modulations and response peaks, as typical also for traditional GLMs[27,59]; and second, it showed typical boundary artifacts often associated with splines, which manifested as increased variance at the left side of some kernels, in particular for running modulated neurons (Figures 2E–2H and S6I–S6L). Despite these challenges, incorporating running information proved beneficial, as confirmed by the permutation test (Figure S6G). These running modulated neurons showed reduced response reliability in repeated stimulus trials (Figures S6M and S6N), which was expected given that their activity was substantially influenced by locomotion state. In line with a previous study,[60] we found that run-modulated neurons as identified by our model had overall low firing rates (Figure S6O).

Is the contribution of modulatory inputs to dLGN neurons' activity consistent and strong enough to improve the prediction of dLGN responses? While dLGN has long been known to exhibit state-dependent changes in firing[11,15,18,61] and to receive extensive feedback from cortex,[5,62] the impact of these influences, in particular during the viewing of naturalistic stimuli, is not well understood. Thus, to quantitatively assess the contributions of CT feedback suppression and behavioral variables, we compared the performance between our model including all inputs and reduced variants of the model with only a subset of inputs (Figures 3A and 3B). Starting with the "Stimulus only" model that only considered the stimulus as input, we found that incorporating one or more modulatory inputs increased the correlation between observed and predicted dLGN responses (ANOVA: $p = 0.022$; Figure 3A). In particular, adding pupil size or a combination of two or more modulatory predictors showed a significantly better performance than the "Stimulus only" model ("Stimulus only" vs. "Stimulus + Pupil size": 0.186 vs. 0.235, Wilcoxon signed-rank test: Bonferroni corrected $p = 3.39 \times 10^{-6}$; "Stimulus only" vs. "Full model": 0.186 vs. 0.249, Wilcoxon signed-rank test: Bonferroni corrected $p = 2.08 \times 10^{-7}$; Figure 3A). Note that even in the full model, we still observed neurons with suboptimal predictions, maybe due to low response reliability (Figure S6N) and sparse firing (Figures S6O and S7H).

Indeed, when we compared the prediction performance of the "Stimulus-only" model with the "Full model" (Figure 3B), we noticed that the inclusion of the modulatory inputs did not merely shift the distribution to higher performances. Instead, a closer examination allowed us to identify a subgroup of neurons whose responses could be predicted only poorly by the visual stimulus, but which showed substantial improvements in their response prediction with the inclusion of modulatory inputs (Figures 3C–3E; we call them the "modulation-sensitive" group; Figures S7A–S7G). In contrast, another subgroup showed no improvement when we added the modulatory inputs

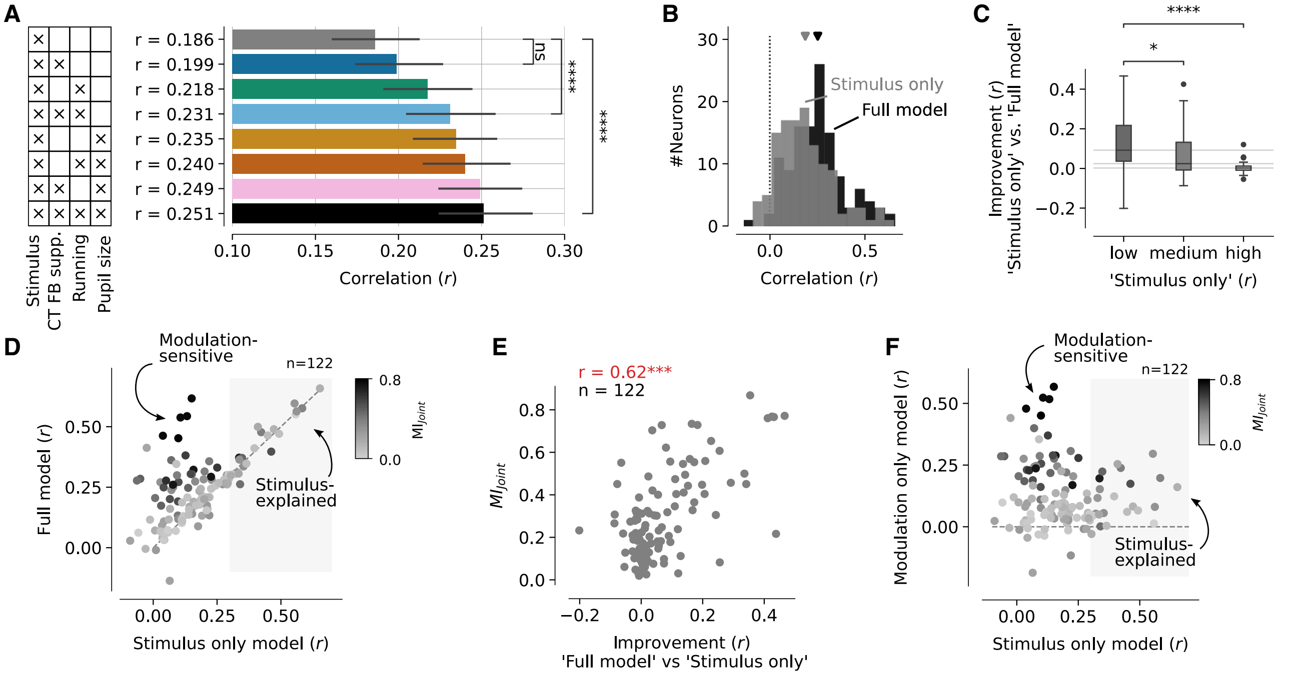

Figure 3. Adding model predictors for modulatory inputs improves the performance for a subgroup of poorly visually responsive dLGN neurons

(A) Comparison of model performance for models with different sets of inputs indicated in the table on the left, sorted by performance. Bonferroni corrected p-values of paired Wilcoxon signed-rank test: $****\ p \leq 1.0 \times 10^{-4}$; “ns” non-significant. Error bars: 95% confidence intervals.

(B) Comparison of model performance (Pearson’s r) for the “Full model” (*black*, inputs: stimulus, CT feedback suppression, run speed, pupil size) and the “Stimulus only” model (*gray*). *Arrow heads*: mean performance (n = 122 neurons).

(C) Improvement in model performance (“Full model”−“Stimulus only”) for neurons grouped by their performance of the “Stimulus only” model. Bonferroni corrected p-values of paired Wilcoxon test: $*p \leq 0.05$; $****\ p \leq 1.0 \times 10^{-4}$. *Dotted lines* indicate the mean of each group. The box displays the quartiles of the distribution, the whiskers represent its range, excluding outliers.

(D) Comparison of model performance for all neurons in the “Stimulus only” model and the “Full model.” Arrows indicate the group of neurons that benefits from adding CT feedback, running, and pupil size (“Modulation-explained”) and the group that does not improve (“Stimulusexplained”).

(E) Relationship between the amount of joint modulation by CT feedback, running, and pupil size estimated directly from the data without a model (see STAR Methods), and the improvement in model performance when adding predictors for modulatory inputs (“Full model”−“Stimulus only”).

(F) Comparison of model performance for the “stimulus only” model and a model without the stimulus (“modulation only”). Arrows indicate “modulation-explained” and “stimulus-explained” neurons. In panels (D, F), darker colors indicate stronger joint modulation by CT feedback, running, and pupil size (MI_{Joint}) estimated directly from the data without a model (see STAR Methods). Panels (D–F) show data from all n = 122 neurons.

(Figures 3C–3E; “stimulus-explained” group). To test the extent to which this might reflect a ceiling effect in explainable variance, we fitted models that contained only modulatory inputs but not the stimulus (“CT FB supp.” + “Running” + “Pupil size”; “Modulation only” models; Figure 3F). For these models, the “modulation-sensitive” neurons still exhibited relatively high performance (Figure 3F, *dark dots*), and the “stimulus-explained” group had lower performance, although not zero (Figure 3F, *light gray dots*). This indicates that even in the “Stimulus-explained” group, modulatory inputs might have some, albeit generally weak effect that was obscured in the full model; alternatively, some modulatory inputs if considered in the “modulation only” models might contain stimulus information, in particular pupil size, which is known to be related not only to arousal, but also to stimulus brightness (Figure S3C). Taken together, our analysis of model performance suggests that dLGN neurons are explained by the visual stimulus, behavior, and CT feedback, albeit with considerable heterogeneity.

Corticothalamic feedback is enhanced in the absence of a patterned visual stimulus

Our model showed only a relatively small subset of dLGN neurons with significant effects of CT feedback. Could the reason for this be that the responses elicited by the rich naturalistic movie stimulus might have dominated dLGN activity relative to the effects of CT feedback? We thus predicted that CT feedback effects might be stronger without patterned stimulus input (Figure 4A).

To test this prediction, we expanded our analyses to the period of blank screen stimulation flanking the movie presentation, and compared the effects of CT feedback suppression in the recorded data and in models fit separately to responses during movies vs. blank periods (Figure 4B). Consistent with our prediction, we indeed observed that CT feedback suppression reduced the firing rates of individual example neurons more strongly during blanks ($MI_{\text{CT FB supp.}}$: −0.65, Figure 4C$_1$) compared to movies ($MI_{\text{CT FB supp.}}$: −0.45, Figure 4C$_2$). This

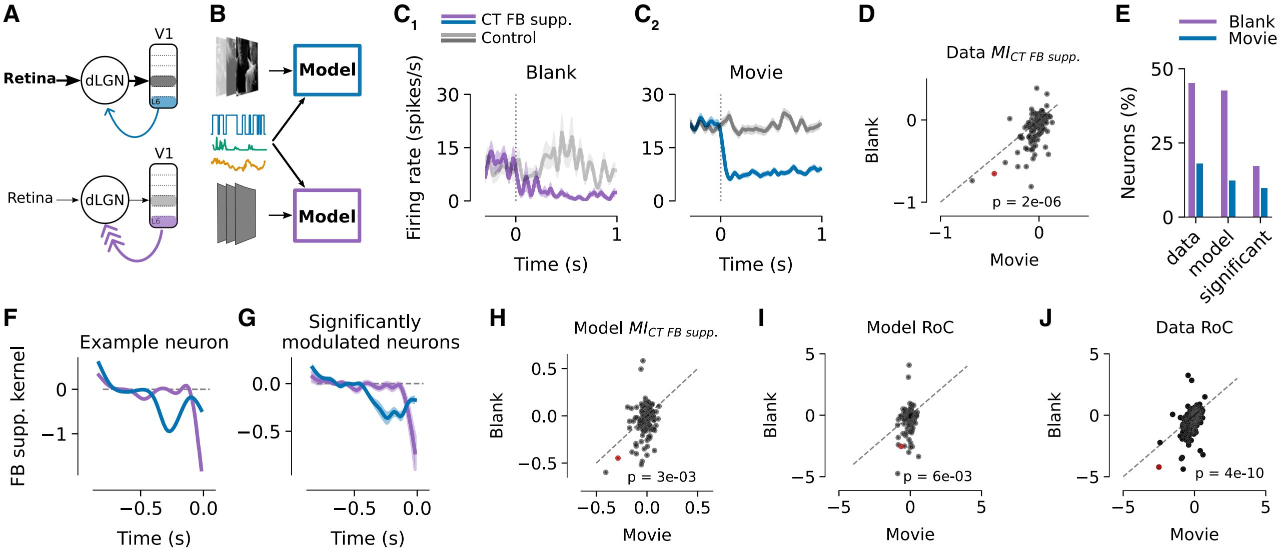

Figure 4. The effect of CT feedback is dependent on the presence or absence of the visual stimulus

(A) Schematics of the hypothesis that the absence of a patterned visual stimulus elicits weaker stimulus-driven input to dLGN, which is in turn accompanied by stronger CT feedback. Note that the schematics should not imply stronger L6 CT pyramidal neuron firing, but that the net effect of CT feedback on dLGN firing is stronger in the absence of a patterned visual stimulus.

(B) Schematics of fitting the spline-GLM model separately during movies (*top*) vs. blank periods (*bottom*).

(C) Effects of CT feedback suppression. (C_1) Mean PSTHs time locked to the onset of photosuppression for one example dLGN neuron (same example neuron as in Figures 1D and 1E) during blank periods (gray screen) flanking the movie presentation. The shaded area represents the SEM. (C_2) Same as (C_1), during movie presentation. *Purple, blue*: PSTH during CT feedback suppression (OFF-ON transition), *light gray, dark gray*: PSTH during control condition (OFF-OFF transition).

(D) Comparison of $MI_{\text{CT FB supp.}}$ during blanks vs. movies for the recorded dLGN population (number of neurons $n = 122$). Note that the results do not depend on the exact metric used for the comparison of CT feedback suppression effects, and also hold if raw differences or simple ratios are considered instead of the $MI_{\text{CT FB supp.}}$

(E) Percentage of recorded dLGN neurons modulated by CT feedback during the two stimulus conditions. Three modulation metrics were separately considered to count the modulated neurons. A neuron was considered modulated (1) based on data: $|MI_{\text{CT FB supp.}}|$ from (D) ≥ 0.1, (2) based on model predictions: $|MI_{\text{CT FB supp.}}|$ from (H) ≥ 0.1, or (3) based on model performance: permutation test $p \leq 0.05$. Notably, all three modulation metrics consistently revealed a higher proportion of neurons displaying CT feedback modulation during the blank condition compared to the movie condition.

(F) CT feedback suppression kernel for the example dLGN neuron in (C_1). The model was trained on either the data during movie presentation (*dark blue*) or blank periods (*light blue*).

(G) Same for all significantly CT feedback modulated neurons ($n_{\text{movie}} = 12$, $n_{\text{blank}} = 21$). Solid lines represent the mean of the kernels, and transparent surrounds represent the standard error of the mean (SEM).

(H) Comparison of $MI_{\text{CT FB supp.}}$ for blanks vs. movies calculated from simulated data using the fitted model for the dLGN population to the two stimuli.

(I) Comparison of the Rate of Change (RoC) of model-predicted neurons' responses to CT feedback suppression during movie presentation vs. blank periods.

(J) Same as (I), for the recorded data. Panels (H–J) show data from all $n = 122$ neurons.

observation held true across the recorded dLGN population (mean $MI_{\text{CT FB supp.}}$ −0.09 vs. −0.03; $p = 2.5 \times 10^{-6}$, Wilcoxon signed-rank test; Figure 4D), and did not depend on the exact metric used for quantifying the differential effect size of CT feedback suppression (difference, ratio, or MI). Furthermore, during blank periods, more dLGN neurons were affected by the suppression of CT feedback (45% vs. 18% with $|MI_{\text{CT FB supp.}}| \geq 0.1$; Figure 4J). The stronger effect of CT feedback suppression could not be explained by the difference in overall firing rate between the two stimulus conditions (Figures S8A and S8B), nor was it related to the different number of optogenetic pulses (Figure S8C).

Is the stronger modulation by CT feedback suppression during blank periods vs. movies also captured by our spline-GLM model? We indeed found that the model learned a more negative CT feedback suppression kernel for the blank condition compared to the movie, both in the example neuron (peak amplitude −1.8 vs. −0.94; Figure 4F) as well as in the population of neurons with a significant CT feedback suppression kernel (−0.86 vs. −0.46, $p = 0.044$, Mann-Whitney-U test, Figure 4G; all neurons: −0.4 vs. −0.2, $p = 5 \times 10^{-8}$, Wilcoxon signed-rank test). To avoid potential confounds of firing rates on kernel amplitudes (Figures S8D and S8E) and enable a more direct comparison to the recorded data, we used the model predictions in the two stimulus conditions and calculated model-derived $MI_{\text{CT FB supp.}}$, analogously to those based on the recorded data. Consistent with our data-driven observations, we found that CT feedback suppression reduced modeled responses more strongly during the blank periods (modeled $MI_{\text{CT FB supp.}}$, −0.057) compared to movies (−0.017; $p = 0.002$, Wilcoxon signed-rank test, Figure 4H).

Inspecting the learned model kernels (Figures 4F and 4G) suggested that, besides amplitude, the dynamics of the CT

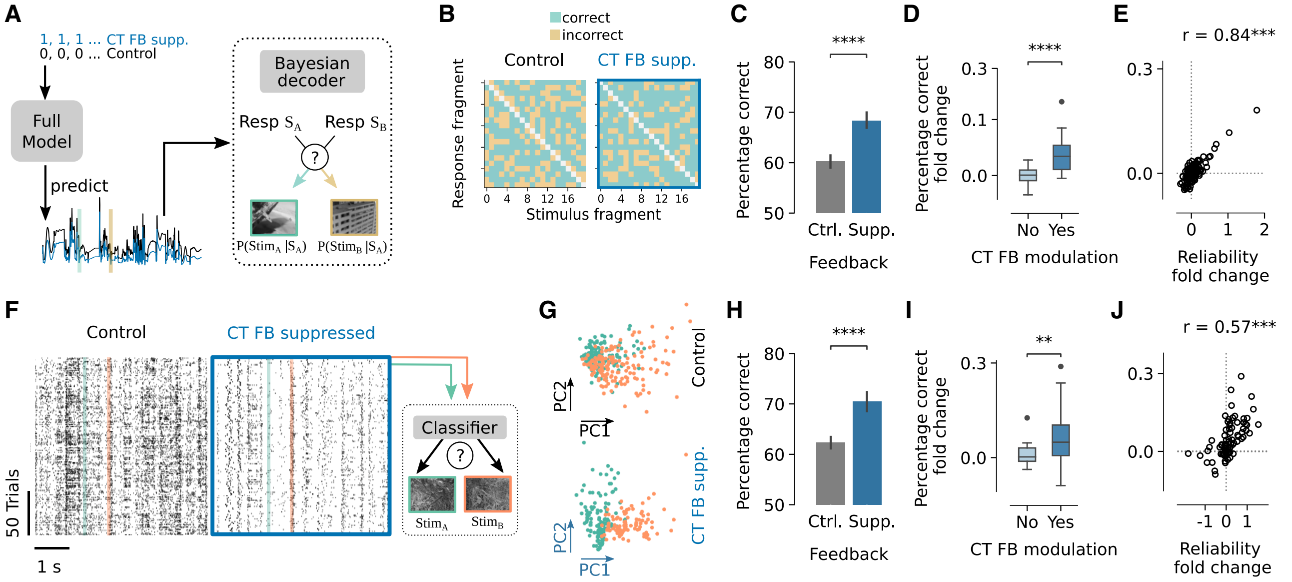

Figure 5. 2AFC decoder applied to modeled and recorded dLGN responses reveals that CT feedback suppression can improve stimulus discrimination

(A) Schematics of the decoder: the trained model was used to simulate responses with CT feedback being either on (*blue*) or off (*black*; 70 s example trace). The movie stimulus, running, and pupil inputs remained the same between CT feedback on and off, using recorded data. Random 50 ms stimulus fragments (*Green*: *A* and *yellow*: *B*) were chosen, each with the corresponding simulated responses. The decoder's task was to determine which stimulus was more likely based on the observed responses. The decision of the decoder was directly derived from the model likelihood for the correct and incorrect pairing[31] (see STAR Methods).

(B) Decision matrix for one example neuron with 20 random stimulus fragments and their simulated responses. *Green*: correct pairing of stimulus and response; *yellow*: incorrect pairing. *Left*: control condition; *right*: CT feedback suppressed condition.

(C) Percentage of correct decisions in the control and the CT feedback suppressed condition, same example modeled neuron as in (B). Error bars indicate 95% confidence intervals.

(D) Change in decoder performance during CT feedback suppression vs. control conditions, split according to whether the modeled neurons were significantly modulated by CT feedback suppression (*dark blue*) or not (*light gray*). The box displays the quartiles of the distribution, the whiskers represent its range, excluding outliers.

(E) Relationship between the fold change in trial-by-trial reliability and the fold change in decoding accuracy with CT feedback suppression across the population of dLGN neurons, obtained from the simulated responses in (A–D).

(F) Spike rasters for one dLGN example neuron in response to a 5 s natural movie clip during the control condition (*left*) and CT feedback suppression (*middle*), obtained from the published dataset by Spacek et al. (2022).[10] *Green/orange shading*: two random 50 ms, non-overlapping movie fragments used to illustrate the analysis. *Right*: illustration of the support vector machine (SVM) trained to perform 2AFC discrimination of the movie fragments based on single-trial responses.

(G) Principal component analysis of the single trial responses to two random 500 ms movie fragments.

(H) Percentage of correct decisions of the SVM trained on the example neuron's responses to 200 random movie fragment-pairs for held-out trials not used for training, separately for the control condition and during CT feedback suppression. Error bars indicate 95% confidence intervals.

(I) Change in SVM discrimination accuracy during CT feedback suppression vs. control conditions, split according to whether the modeled neurons were significantly modulated by CT feedback suppression (*dark blue*) or not (*light gray*). Modulated neurons were defined as the neurons whose firing rates were significantly negatively modulated by CT feedback suppression ($p \le 0.01, n = 200$ trials, Mann-Whitney-U test). The box displays the quartiles of the distribution, the whiskers represent its range, excluding outliers.

(J) Relationship between the fold change in trial-by-trial reliability and the fold change in decoding accuracy across the population of dLGN neurons, obtained from the published dataset by Spacek et al. (2022)[10] in (F–I). Error bars indicate 95% confidence intervals. Significant results are indicated with $^{**}p \le 0.01$, $^{***}p \le 0.001$ and $^{****}p \le 0.0001$.

feedback suppression effects might also differ between visual stimulus conditions. Specifically, the spline-GLM learned a kernel characterised by a faster and briefer time course for blank periods compared to movie stimulation. This observation could be quantified by calculating the rate of change (RoC) of the neurons' predicted and actual responses after photosuppression (see STAR Methods). Indeed, we found that the effect of CT feedback suppression was faster during blank periods (model-based RoC: $p = 0.004$, Wilcoxon signed-rank test, Figure 4I; data-based: $p = 9 \times 10^{-12}$, Wilcoxon signed-rank test; Figure 4J). In conclusion, the fitted splineGLM models revealed that the observed impact of CT feedback suppression was weaker and slower during the presence of a rich patterned visual stimulus in comparison to blank periods, suggesting that the observed effect of CT feedback depends on the visual stimulus characteristics.

Corticothalamic feedback suppression can improve stimulus discrimination

Finally, we sought to understand how suppressing CT feedback affected the representation of visual information in the dLGN (Figure 5). To do so, we evaluated the performance of a decoder

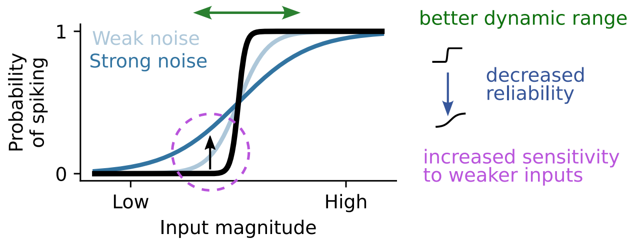

Figure 6. Synaptic noise framework of CT feedback

Schematic illustration of the framework by Wolfart et al. (2005)[40] and Behuret et al. (2015),[41] proposing that CT feedback induced synaptic noise could tune the transfer function of individual dLGN neurons, making them more sensitive to weaker inputs. The noise-induced increased sensitivity, however, comes at the expense of making action potential firing more probabilistic, thus decreasing single-neuron reliability. Such decreased single-neuron reliability could be offset through the strong convergence at the geniculo-cortical synapse,[63–65] where the pooled afferent signal would not only have increased sensitivity to weak inputs, but also an increased dynamic range and hence better resolution. Adapted from Behuret et al. (2015), originally published under a Creative Commons Attribution License (CC BY).

applied to individual dLGN neurons, comparing its ability to discriminate between movie fragments during CT feedback suppression and the control condition with intact feedback.

To isolate the effects of CT feedback suppression on the representation of stimulus information, we used an *in silico* approach based on our trained model (“Full model”) (Figure 5A). By selectively changing CT feedback suppression, while keeping the visual stimulus, running and pupil inputs the same across CT feedback conditions, we conducted a decoding experiment based on the simulated model responses to distinguish between video clips in a two-alternative forced choice (2AFC) setting. We randomly selected 50 ms fragments of stimulus-responsepairs from the test set that had not been used for model fitting. To discriminate between two movie clips, we used the maximum-likelihood decoding rule from Pillow et al. (2005)[31] (see STAR Methods). The decision of the 2AFC decoder was directly derived from the model likelihood for the correct and incorrect pairing.[31] We considered the decision correct if a Bayesian decoder assigned a higher likelihood to the correct pairing than the incorrect pairing. We found that the decoder achieved more correct decisions in the CT feedback suppressed condition compared to the control condition (Figure 5B, 20 representative stimulus-response pairs for one example neuron; Figure 5, across all 100 stimulus pairs: 68.3% vs. 60.3%, $p = 1.20 \times 10^{-12}$, Wilcoxon rank-sum test).

To quantify how well each modeled neuron distinguished between movie fragments, we calculated the change in decoding success between the CT feedback-suppressed and control conditions (Figure 5D). For neurons without significant CT feedback kernel, the change in decoding was near zero, suggesting little difference in stimulus information between CT feedback suppression and control conditions (average 0.006 ± 0.01, mean ± SD; Figure 5D, gray; Figure S9A). However, for CT feedback modulated neurons, decoding success was significantly higher in the CT feedback suppressed condition than the control condition ($p = 0.002$, Wilcoxon rank-sum test, average change in decoding success 0.05 ± 0.05, mean ± SD; Figure 5D, blue; Figure S9A). Furthermore, the change in decoding accuracy was higher in the population of CT feedback modulated neurons in comparison to non-modulated neurons ($p = 4.35 \times 10^{5}$, MannWhitney-U test; Figure 5D). We found that this increase in decoder accuracy during CT feedback suppression was highly correlated to response reliability of the simulated trials (Pearson’s $r = 0.84$, $n = 122$, $p = 5.9 \times 10^{-33}$; Figure 5E). Thus, our model predicted that with CT feedback “on,” short duration activity of individual dLGN neurons can carry less information about the visual stimulus.

To test the prediction of our *in silico* experiment regarding the potential for improved decoding during CT feedback suppression, we analyzed a published dataset.[10] This dataset includes responses of dLGN neurons to a large number of repeated presentations of a natural movie clip under two conditions: a control condition and a condition with CT feedback suppression (Figure 5F, *left* and *right*). We first visualized the distinctiveness of single trial responses to two randomly selected 500 ms time windows and found that responses during CT feedback suppression appeared to be more separable compared to the control condition (Figure 5G). Encouraged by these results, we then used a support vector machine (SVM) classifier (see STAR Methods) with settings mimicking those applied to the simulated data, to discriminate in a 2AFC setting single trial responses between randomly selected 50 ms movie fragments (Figure 5F). Consistent with our *in silico* predictions, the SVM decoder achieved higher accuracy in the FB suppressed condition compared to the control condition, for both the example neuron (70.5% vs. 62.4%, $p = 6.07 \times 10^{-11}$, Mann-Whitney-U test; Figure 5H) and for the subpopulation of CT feedback modulated vs. non-modulated neurons ($p = 9.6 \times 10^{-3}$, Mann-Whitney-U test; Figures 5I and S9B). Similar results were obtained for different fragment durations (Figures S9C–S9E).

Finally, in accordance with our results for the simulated data, we also found that for the published dataset, improvements in decoding accuracy with CT feedback suppression were associated with enhancements in trial-by-trial reliability (Pearson’s $r = 0.57$, $n = 78$, $p = 3.59 \times 10^{-8}$, Figures 5J, S9F, and S9G). Taken together, both our simulations and analysis performed with an independent dataset suggest that CT feedback can impair the representation of visual stimulus information in individual dLGN neurons, which seems to be related to their reduced trial-by-trial response reliability with CT feedback intact.

How could this counter-intuitive result be explained? One possibility could be a framework suggested by previous research[40,41] according to which CT feedback could linearize the input output relationship of thalamic neurons through the injection of synaptic noise (Figure 6). This linearization would enhance the excitability of thalamic neurons to weaker inputs, in line with the stronger CT feedback effects for blanks vs. movies, but would additionally push them into more unreliable, probabilistic firing regimes (Figure 6), in line with our observation of worse single-neuron decoding performance with CT feedback. Importantly, such increased variability in individual dLGN neurons could still be useful for visual processing, as it might be offset and even exploited by the strong convergence in the thalamocortical system.[63–65] Specifically, synaptic noise mediated by CT feedback might allow V1 L4 neurons to extract from the pooled afferent signal stimulus-related information not only with enhanced sensitivity to weaker inputs but also with a larger dynamic range and hence better resolution.[40,41] Alternative explanations for the increased trial-by-trial variability could include that CT feedback conveys cortical representations of variables to dLGN that are uncontrolled between trials in our experimental settings and benefit vision beyond stimulus decoding.

DISCUSSION

Here, we quantitatively characterized how dLGN responses during the viewing of a naturalistic movie are influenced by the combination of visual stimulus-related inputs, CT feedback, and behavioral state. We modeled the responses of individual dLGN neurons using a data-efficient GLM, which predicted the spatiotemporal RFs and response modulations by CT FB suppression, the animal's run speed, and pupil size. We found that overall model performance improved when including the modulatory predictors, in particular for a subpopulation of dLGN neurons whose responses were poorly explained by the visual stimulus. Guided by the model, we found that the effect of CT FB suppression depended on stimulus type, being relatively stronger, more prevalent, and faster in the absence of a patterned visual stimulus. Finally, our model predicted that the responses of a subset of CT-feedback-sensitive dLGN neurons contained more visual information when CT feedback was suppressed, which we verified in a published dataset. Together, our results show that the activity of dLGN neurons is influences by a combination of stimulus-driven and modulatory inputs, whose relative impact depends on visual responsiveness and stimulus type, with CT feedback affecting sensitivity and variability potentially to tune the thalamic relay.

Using a spline-generalized linear models for modeling thalamic responses

Our work extends previous approaches that the modeled thalamic processing of naturalistic visual stimuli (e.g.,[37,38,66]). In particular, our framework allowed us to test model variants with different combinations of predictors, which revealed a subpopulation of dLGN neurons whose responses were poorly predicted by the movie stimulus and more strongly affected by the modulatory inputs. These might correspond to a previously reported set of neurons in mouse dLGN, amounting to 30–40%,[58,67] with poor or unclear visual feature selectivity. Given that this subpopulation also contained an over-representation of low-firing neurons, their relatively stronger modulation (see also Dearnley et al., 2023[60]) might be indicative of a tight excitatory/inhibitory (E/I) coupling in the recorded network.[68] Such tight E/I coupling in the thalamo-cortico-thalamic network might be mechanistically achieved through feedforward and feedback inhibition by inhibitory neurons in dLGN and the thalamic reticular nucleus, respectively, and the joint modulation of thalamic neurons by CT feedback and neuromodulation.[1,4,7,9]

The general success of our model is indicated by the close neuron-by-neuron correspondence between RF properties and response types derived from the model and more traditional analyses and stimuli, and by the prominent relationship between learned model kernels and data-driven modulation indices for CT feedback suppression, run speed and pupil size. Yet, while our data-driven modulation indices generally matched well with the magnitudes of modulatory influences previously observed in mouse dLGN,[7,10,11,14,18] we were surprised to find only a relatively small fraction of dLGN neurons with significant kernels for CT feedback suppression, running, and pupil size. Reasons for the small fraction might be at least 3-fold: (1) the conservative method for assessing significance in the model derived from session-based permutation tests,[54] (2) the continuous nature of inputs to the model rather than a split into extreme conditions for some of the modulation indices (e.g., sit vs. run while excluding transition states), (3) the direct suppression of L6 CT feedback through the soma-targeted, light-gated chloride channel stGtACR2,[42] which might have yielded comparatively weaker effects (see also[10,69]) than alternative approaches recruiting powerful intracortical inhibition through the photostimulation of inhibitory V1 neurons.[6,7,9,10,69,70]

In the future, our spline-GLM could be extended by thalamic mechanisms, such as the fast adaptation of integration time according to luminance and contrast,[66,71] accounting for the constant changes in spatial and temporal integration elicited by dynamic natural stimuli.[72] Further, by combining the model inputs, one could test for interactions, for instance to clarify the dependence of CT feedback effects and behavioral state-related modulations as proposed by some studies.[69] Incorporating adaptive amplitudes of input and post-spike kernels[73] could differentiate tonic and burst spiking behaviors, characteristic of thalamic neurons[74] and known to be affected by both stimulus-related[75] and modulatory inputs.[10,11,15,61] Finally, alternative modeling approaches based on deep neural networks (DNNs)[76–78] promise to better capture non-linear dynamics and faster transients, potentially enhancing our capabilities to capture neuronal responses and complex neural interactions, yet likely at the expense of interpretability and uncontrolled biases.[79,80]

Spatiotemporal RFs and modulatory inputs of mouse dorsolateral geniculate nucleus neurons

Through a combination of analyzing receptive fields obtained from the model using a naturalistic movie stimulus, a noise stimulus, and more traditional RF mapping techniques, we identified both expected and unexpected types of dLGN spatiotemporal RFs. Indeed, consistent with previous studies quantifying RFs in mouse dLGN to simple stimuli,[55–58] our model learned circular spatial RFs for the majority of neurons, which often consisted of a single domain resembling the well-known ON and OFF fields. Reminiscent of a study showing that retinal ganglion cells can reverse the polarity of their RFs in response to different natural images,[81] we found that some dLGN neurons had an opposite RF polarity when characterized with simple luminance steps or the movie stimulus. Finally, some of the RFs obtained with our modeling approach had a complex spatial structure, and might thus correspond to a subset of dLGN neurons that had been previously noted to lack clearly localized RFs.[56,58] Future studies, for instanced based on the "maximally exciting image" approach initially applied to mouse V1,[82] are needed to verify to which degree these complex RF structures indeed reflect complex feature selectivity of dLGN neurons or might be potential consequences of the modeling approach.

Despite its frequent portrayal as a relay station, the dLGN of the thalamus has long been recognized as one of the earliest stages in the visual system that integrates visual representations with additional information.[3,4,12,15,83] Corroborating this, we found that the performance of our model generally improved with the inclusion of modulatory inputs, albeit with considerable neuron-by-neuron diversity. Previous studies have already reported differential effects of behavioral state and arousal, and could relate them to the neurons' feature selectivity.[18,19,84] In dLGN, the firing of neurons with non-linear responses to high spatial frequencies and with transient ON responses seem preferentially enhanced by locomotion.[18] In addition, retinal boutons preferring low spatial frequencies and luminance decrements seem preferentially suppressed by arousal.[19] The neuron-by-neuron diversity in the impact of the modulatory inputs might thus serve to enhance particular visual inputs during active states.

Corticothalamic feedback effects on single dorsolateral geniculate nucleus neuron stimulus encoding and decoding

Our observation of faster and relatively stronger CT feedback effects during blank periods compared to movie viewing contributes to the growing appreciation that CT feedback effects on dLGN firing rates seem to be stimulus-dependent, and potentially overridden by strong visual stimulation (see also[10,85]). Indeed, the effect of CT feedback seems to be most potent in the absence of patterned stimulus input, both in mice (this study and[10,44] for related findings with gratings) and ferrets,[85] which might point to a common mechanism across species. Across all these studies without patterned visual stimulus, CT feedback had a net enhancing effect. Similarly, also our previous work in Born et al.,[7] although largely focusing on suppressive effects of CT feedback for large-sized gratings, observed enhancing effects of CT FB during blank screen conditions (and for small-sized gratings). We propose that the observed greater influence of CT feedback suppression during spontaneous activity than movie viewing could arise from a differential engagement of direct excitatory and inhibitory feedback pathways during these visual stimulus types. Supplying thalamic relay neurons with different ratios of excitatory and inhibitory conductances, mimicking the impact of modulatory inputs, can shift their input/output function, such that the same somatic input can generate markedly different spiking responses.[40,41] Future studies will need to use more subtle manipulations of stimulus type, including contrast and spatial structure, together with pathway-specific CT feedback suppression, to test the hypothesis that CT feedback might be most effective with weak visual inputs, as potentially encountered during challenging sensory conditions. In addition, future studies will profit from simultaneous recordings of V1 and dLGN to further disentangle the origin and potential interaction of CT feedback and other modulatory influences.

Besides relatively stronger and faster CT feedback effects on dLGN firing rates in the absence of a patterned visual input, we also observed that CT feedback could reduce single-trial information in individual dLGN neurons about the visual stimulus. This result might at first glance seem counter-intuitive given prior research associating cortico-cortical feedback with attention and enhancements of stimulus encoding (e.g.,[86–90]). Both enhanced sensitivity to weak inputs and decreased reliability of firing in individual dLGN neurons are core ideas of a framework proposing that one function of CT feedback might be to linearize the input-output relationship of thalamic neurons through the injection of synaptic noise.[40,41] This linearization would enhance the excitability of thalamic neurons to weaker inputs, at the expense of pushing them into more unreliable, probabilistic firing regimes. The predictions of the noise framework of CT feedback[40,41] would thus be in line with both of our results regarding the stronger impact of CT feedback during blank stimuli than movies and the decreased trial-by-trial reliability and compromised single-neuron stimulus decoding.

How could a CT feedback induced decrease in single-neuron reliability serve vision? The synaptic noise framework of CT feedback[40,41] proposes that increased variability in individual dLGN neurons could be offset and even exploited by the strong convergence in the thalamocortical system.[63–65] Specifically, synaptic noise mediated by CT feedback might allow to extract from the pooled afferent signal stimulus-related information not only with enhanced sensitivity to weaker inputs but also with a larger dynamic range and hence better resolution.[40,41] Thus, in the future, a more realistic decoder would consider local populations of thalamocortical neurons, to test the hypothesis that, through CT feedback mediated synaptic noise, cortex enhances both its sensitivity to ambiguous inputs and its resolution of the stimulus representation, through the linearization of the pooled afferent thalamic inputs. Note that this framework relies not only on strong thalamocortical convergence, but also on the feedback-mediated synaptic noise being at least somewhat statistically independent across dLGN neurons. This would need to be tested in future experiments suppressing CT feedback during recordings of large populations of single dLGN neurons.

In conclusion, our results add to the growing body of evidence that dLGN activity is influenced not only by visual inputs but also by modulatory influences from CT feedback and behavioral state. Our work presents an important step toward a quantitative understanding of how dLGN responses to complex, naturalistic stimuli are shaped by the simultaneous influences of stimulus related feedforward inputs, CT feedback and behavior.

Limitations of the study

There are also several limitations in our study. First, the amount of expression and optogenetic light placement for CT feedback suppression was not exactly the same across each mouse. This may result in variable results. More importantly, firing mode of thalamic neurons, i.e., tonic and burst mode, an important target for neuromodulation and CT feedback, was not considered in our analysis. Second, we attempted to adjust our GLM by replacing the soft plus nonlinearity with an exponential nonlinearity to better reflect the known gain modulations of CT feedback and behavioral state,[28] instead of modeling them as additive effects. However, this approach led to instability during model training, thus preventing us from using the exponential nonlinearity. The model and its simulated responses thus can not fully capture the neuronal mechanisms underlying response modulations by CT feedback and behavioral state. Lastly, effects of CT feedback and behavioral state might be different under freely moving conditions and in a task context. Both aspects require further investigation.

RESOURCE AVAILABILITY

Lead contact

Requests for further information and resources should be directed to and will be fulfilled by the lead contact, Laura Busse (busse@bio.lmu.de).

Materials availability

This study did not generate new materials.

Data and code availability

- Data: All electrophysiological, behavioral, model-related data have been deposited at Zenodo under https://doi.org/10.5281/zenodo.15478978 and are publicly available as of the date of publication. The DOI is listed in the key resources table.
- Code: All original code has been deposited at Zenodo under https://doi.org/10.5281/zenodo.15479878 and is publicly available as of the date of publication. The DOI is listed in the key resources table.
- Any additional information required to reanalyze the data reported in this article is available from the lead contact upon request.

ACKNOWLEDGMENTS

This research was supported by the Deutsche Forschungsgesellschaft (DFG) Sonderforschungsbereich (SFB) 1233, Robust Vision: Inference Principles and Neural Mechanisms, Teilprojekt (TP) 13, project number: 276693517 (L.B., P. B.), by SPP 2041 (BU 1808/6-1 and BU 1808/6-2; L.B.), the RTG 2175 “Perception in context and its neural basis” (L.B.) and the Hertie Foundation (P.B.). Lisa Schmors was supported by the International Max Planck Research School for Intelligent Systems (IMPRS-IS), Lukas Meyerbolbersleben was supported by an Add-On Fellowship from the Joachim Herz Foundation. We thank E. Froudarakis (A. Tolias Lab, Baylor College of Medicine, Houston, TX) for providing of the movie stimulus files, S. Renner for helping with the database implementation, and A. Ecker and T. Euler for the discussion of the stimulus design. In addition, L.B. thanks M. Sotgia for lab management and support with animal handling and histology, S. Schörnich for IT support, and B. Grothe for providing excellent research infrastructure.

AUTHOR CONTRIBUTIONS

Conceptualization, L.B., P.B., and S.S.; methodology, L.S., Y.B., A.K., Z.H., D. C. P.B., S.S., and L.B.; software, L.S., A.K., Y.B., Z.H., and D.C.; formal analysis, L.S., A.K., and Y.B.; investigation, Y.B., A.K., and L.M.; resources, L.B. and P.B.; data curation, L.S., A.K., Y.B., L.M., and D.C.; writing – original draft, L.B., L.S., A.K., and Y.B.; writing – review and editing, all authors; visualization, L.S., A.K., and Y.B.; supervision, L.B., P.B., and S.S.; project administration, L. B. and P.B.; funding acquisition, L.B. and P.B.

DECLARATION OF INTERESTS

The authors declare no competing interests.

STAR★METHODS

Detailed methods are provided in the online version of this paper and include the following:

- KEY RESOURCES TABLE
- EXPERIMENTAL MODEL AND SUBJECT DETAILS
- METHOD DETAILS
  - ○ Surgical procedures
  - ○ Extracellular recordings
  - ○ Locomotion
  - ○ Eye tracking
  - ○ Optogenetic feedback suppression
  - ○ Joint modulation by additional inputs
  - ○ Visual stimulation
  - ○ Histology
- QUANTIFICATION AND STATISTICAL ANALYSIS
  - ○ Spike sorting and unit extraction
  - ○ Unit quality metrics
  - ○ Neuronal data analysis
  - ○ Reliability of CT feedback suppression
  - ○ Spline-based generalized linear model
  - ○ Spatio-temporal RF characterization
  - ○ Cell types clustering
  - ○ Decoding analysis

SUPPLEMENTAL INFORMATION

Supplemental information can be found online at https://doi.org/10.1016/j.isci.2025.112481.

Supporting citation

The following reference appears in the supplemental information: Vinje and Gallant.[91]

Received: January 20, 2025
Revised: March 20, 2025
Accepted: April 15, 2025
Published: May 12, 2025

REFERENCES

1. Guido, W. (2018). Development, form, and function of the mouse visual thalamus. J. Neurophysiol. *120*, 211–225. https://doi.org/10.1152/jn.00651.2017.
2. Usrey, W.M., and Alitto, H.J. (2015). Visual Functions of the Thalamus. Annu. Rev. Vis. Sci. *1*, 351–371. https://doi.org/10.1146/annurev-vision-082114-035920.
3. Weyand, T.G. (2016). The multifunctional lateral geniculate nucleus. Rev. Neurosci. *27*, 135–157. https://doi.org/10.1515/revneuro-2015-0018.
4. Sillito, A.M., Cudeiro, J., and Jones, H.E. (2006). Always returning: feedback and sensory processing in visual cortex and thalamus. Trends Neurosci. *29*, 307–316. https://doi.org/10.1016/j.tins.2006.05.001.
5. Briggs, F., and Usrey, W.M. (2011). Corticogeniculate feedback and parallel processing in the primate visual system. J. Physiol. *589*, 33–40. https://doi.org/10.1113/jphysiol.2010.193599.
6. Olsen, S.R., Bortone, D.S., Adesnik, H., and Scanziani, M. (2012). Gain control by layer six in cortical circuits of vision. Nature *483*, 47–52. https://doi.org/10.1038/nature10835.
7. Born, G., Schneider-Soupiadis, F.A., Erisken, S., Vaiceliunaite, A., Lao, C.L., Mobarhan, M.H., Spacek, M.A., Einevoll, G.T., and Busse, L. (2021). Corticothalamic feedback sculpts visual spatial integration in mouse thalamus. Nat. Neurosci. *24*, 1711–1720. https://doi.org/10.1038/s41593-021-00943-0.
8. Shepherd, G.M.G., and Yamawaki, N. (2021). Untangling the cortico-thalamo-cortical loop: cellular pieces of a knotty circuit puzzle. Nat. Rev. Neurosci. *22*, 389–406. https://doi.org/10.1038/s41583-021-00459-3.
9. Nestvogel, D.B., and McCormick, D.A. (2022). Visual thalamocortical mechanisms of waking state-dependent activity and alpha oscillations. Neuron *110*, 120–138.e4. https://doi.org/10.1016/j.neuron.2021.10.005.
10. Spacek, M.A., Crombie, D., Bauer, Y., Born, G., Liu, X., Katzner, S., and Busse, L. (2022). Robust effects of corticothalamic feedback and behavioral state on movie responses in mouse dLGN. Elife *11*, e70469.

11. Erisken, S., Vaiceliunaite, A., Jurjut, O., Fiorini, M., Katzner, S., and Busse, L. (2014). Effects of locomotion extend throughout the mouse early visual system. Curr. Biol. *24*, 2899–2907. https://doi.org/10.1016/j.cub.2014.10.045.
12. McCormick, D.A. (1992). Neurotransmitter actions in the thalamus and cerebral cortex and their role in neuromodulation of thalamocortical activity. Prog. Neurobiol. *39*, 337–388. https://doi.org/10.1016/0301-0082(92)90012-4.
13. Crombie, D., Spacek, M.A., Leibold, C., and Busse, L. (2024). Spiking activity in the visual thalamus is coupled to pupil dynamics across temporal scales. PLoS Biol. *22*, e3002614. https://doi.org/10.1371/journal.pbio.3002614.
14. Molnar, B., Sere, P., Bord' e, S., Ko' os, K., Zsigri, N., Horv' ath, P., and L' orincz, M.L. (2021).˝Cell type-specific arousal-dependent modulation of thalamic activity in the lateral geniculate nucleus. Cereb. Cortex Commun. *2*, tgab020. https://doi.org/10.1093/texcom/tgab020.
15. Bezdudnaya, T., Cano, M., Bereshpolova, Y., Stoelzel, C.R., Alonso, J. M., and Swadlow, H.A. (2006). Thalamic burst mode and inattention in the awake LGNd. Neuron *49*, 421–432. https://doi.org/10.1016/j.neuron.2006.01.010.
16. Swadlow, H.A., and Weyand, T.G. (1987). Corticogeniculate neurons, corticotectal neurons, and suspected interneurons in visual cortex of awake rabbits: receptive-field properties, axonal properties, and effects of EEG arousal. J. Neurophysiol. *57*, 977–1001. https://doi.org/10.1152/jn.1987.57.4.977.
17. Cano, M., Bezdudnaya, T., Swadlow, H.A., and Alonso, J.M. (2006). Brain state and contrast sensitivity in the awake visual thalamus. Nat. Neurosci. *9*, 1240–1242. https://doi.org/10.1038/nn1760.
18. Aydın, Ç., Couto, J., Giugliano, M., Farrow, K., and Bonin, V. (2018). Locomotion modulates specific functional cell types in the mouse visual thalamus. Nat. Commun. *9*, 4882. https://doi.org/10.1038/s41467-018-06780-3.
19. Liang, L., Fratzl, A., Reggiani, J.D.S., El Mansour, O., Chen, C., and Andermann, M.L. (2020). Retinal inputs to the thalamus are selectively gated by arousal. Curr. Biol. *30*, 3923–3934.e9. https://doi.org/10.1016/j.cub.2020.07.065.
20. Poulet, J.F.A., Fernandez, L.M.J., Crochet, S., and Petersen, C.C.H. (2012). Thalamic control of cortical states. Nat. Neurosci. *15*, 370–372. https://doi.org/10.1038/nn.3035.
21. McClurkin, J.W., and Marrocco, R.T. (1984). Visual cortical input alters spatial tuning in monkey lateral geniculate nucleus cells. J. Physiol. *348*, 135–152. https://doi.org/10.1113/jphysiol.1984.sp015103.
22. Murphy, P.C., and Sillito, A.M. (1987). Corticofugal feedback influences the generation of length tuning in the visual pathway. Nature *329*, 727–729. https://doi.org/10.1038/329727a0.
23. Jones, H.E., Andolina, I.M., Ahmed, B., Shipp, S.D., Clements, J.T.C., Grieve, K.L., Cudeiro, J., Salt, T.E., and Sillito, A.M. (2012). Differential feedback modulation of center and surround mechanisms in parvocellular cells in the visual thalamus. J. Neurosci. *32*, 15946–15951. https://doi.org/10.1523/jneurosci.0831-12.2012.
24. Hasse, J.M., and Briggs, F. (2017). Corticogeniculate feedback sharpens the temporal precision and spatial resolution of visual signals in the ferret. Proc. Natl. Acad. Sci. USA *114*, E6222–E6230. https://doi.org/10.1073/pnas.1704524114.
25. Wang, W., Jones, H.E., Andolina, I.M., Salt, T.E., and Sillito, A.M. (2006). Functional alignment of feedback effects from visual cortex to thalamus. Nat. Neurosci. *9*, 1330–1336. https://doi.org/10.1038/nn1768.
26. Crandall, S.R., Cruikshank, S.J., and Connors, B.W. (2015). A corticothalamic switch: Controlling the thalamus with dynamic synapses. Neuron *86*, 768–782. https://doi.org/10.1016/j.neuron.2015.03.040.
27. Paninski, L. (2004). Maximum likelihood estimation of cascade point-process neural encoding models. Netw. Comput. Neural Syst. *15*, 243–262. https://doi.org/10.1088/0954-898x_15_4_002.
28. Pillow, J.W., Shlens, J., Paninski, L., Sher, A., Litke, A.M., Chichilnisky, E. J., and Simoncelli, E.P. (2008). Spatio-temporal correlations and visual signalling in a complete neuronal population. Nature *454*, 995–999. https://doi.org/10.1038/nature07140.
29. Butts, D.A. (2019). Data-driven approaches to understanding visual neuron activity. Annu. Rev. Vis. Sci. *5*, 451–477. https://doi.org/10.1146/annurev-vision-091718-014731.
30. Paninski, L., Pillow, J., and Lewi, J. (2007). Statistical models for neural encoding, decoding, and optimal stimulus design. In Computational Neuroscience: Theoretical Insights into Brain Function (Elsevier), pp. 493–507. https://doi.org/10.1016/s0079-6123(06)65031-0.
31. Pillow, J.W., Paninski, L., Uzzell, V.J., Simoncelli, E.P., and Chichilnisky, E.J. (2005). Prediction and decoding of retinal ganglion cell responses with a probabilistic spiking model. J. Neurosci. *25*, 11003–11013. https://doi.org/10.1523/JNEUROSCI.3305-05.2005.
32. Steinmetz, N.A., Zatka-Haas, P., Carandini, M., and Harris, K.D. (2019). Distributed coding of choice, action and engagement across the mouse brain. Nature *576*, 266–273. https://doi.org/10.1038/s41586-019-1787-x.
33. Runyan, C.A., Piasini, E., Panzeri, S., and Harvey, C.D. (2017). Distinct timescales of population coding across cortex. Nature *548*, 92–96. https://doi.org/10.1038/nature23020.
34. Park, I.M., Meister, M.L.R., Huk, A.C., and Pillow, J.W. (2014). Encoding and decoding in parietal cortex during sensorimotor decision-making. Nat. Neurosci. *17*, 1395–1403. https://doi.org/10.1038/nn.3800.
35. Musall, S., Kaufman, M.T., Juavinett, A.L., Gluf, S., and Churchland, A.K. (2019). Singletrial neural dynamics are dominated by richly varied movements. Nat. Neurosci. *22*, 1677–1686. https://doi.org/10.1038/s41593-019-0502-4.
36. Goltstein, P.M., Reinert, S., Bonhoeffer, T., and Hübener, M. (2021). Mouse visual cortex areas represent perceptual and semantic features of learned visual categories. Nat. Neurosci. *24*, 1441–1451. https://doi.org/10.1038/s41593-021-00914-5.
37. Babadi, B., Casti, A., Xiao, Y., Kaplan, E., and Paninski, L. (2010). A generalized linear model of the impact of direct and indirect inputs to the lateral geniculate nucleus. J. Vis. *10*, 22. https://doi.org/10.1167/10.10.22.
38. Butts, D.A., Weng, C., Jin, J., Alonso, J.M., and Paninski, L. (2011). Temporal precision in the visual pathway through the interplay of excitation and stimulus-driven suppression. J. Neurosci. *31*, 11313–11327. https://doi.org/10.1523/jneurosci.0434-11.2011.
39. Huang, Z., Ran, Y., Oesterle, J., Euler, T., and Berens, P. (2021). Estimating smooth and sparse neural receptive fields with a flexible spline basis. Neuron. Behav. Data Anal. Theory *5*, 1–14. https://doi.org/10.51628/001c.27578.
40. Wolfart, J., Debay, D., Le Masson, G., Destexhe, A., and Bal, T. (2005). Synaptic background activity controls spike transfer from thalamus to cortex. Nat. Neurosci. *8*, 1760–1767.
41. Behuret, S., Deleuze, C., and Bal, T. (2015). Corticothalamic synaptic noise as a mecha-' nism for selective attention in thalamic neurons. Front. Neural Circ. *9*, 80.
42. Mahn, M., Gibor, L., Patil, P., Cohen-Kashi Malina, K., Oring, S., Printz, Y., Levy, R., Lampl, I., and Yizhar, O. (2018). High-efficiency optogenetic silencing with soma-targeted anion-conducting channelrhodopsins. Nat. Commun. *9*, 4125. https://doi.org/10.1038/s41467-018-06511-8.
43. Gong, S., Zheng, C., Doughty, M.L., Losos, K., Didkovsky, N., Schambra, U.B., Nowak, N.J., Joyner, A., Leblanc, G., Hatten, M.E., and Heintz, N. (2003). A gene expression atlas of the central nervous system based on bacterial artificial chromosomes. Nature *425*, 917–925. https://doi.org/10.1038/nature02033.
44. Kirchgessner, M.A., Franklin, A.D., and Callaway, E.M. (2021). Distinct "driving" versus "modulatory" influences of different visual corticothalamic pathways. Curr. Biol. *31*, 5121–5137.e7.

45. Tsumoto, T., Creutzfeldt, O., and Legendy, C. (1978). Functional organization of the corticofugal system from visual cortex to lateral geniculate nucleus in the cat: With an appendix on geniculo-cortical mono-synaptic connections. Exp. Brain Res. *32*, 345–364. https://doi.org/10.1007/bf00238707.

46. Ichida, J.M., and Casagrande, V.A. (2002). Organization of the feedback pathway from striate cortex (V1) to the lateral geniculate nucleus (LGN) in the owl monkey (aotus trivirgatus). J. Comp. Neurol. *454*, 272–283. https://doi.org/10.1002/cne.10441.

47. Liang, L., Fratzl, A., Goldey, G., Ramesh, R.N., Sugden, A.U., Morgan, J. L., Chen, C., and Andermann, M.L. (2018). A fine-scale functional logic to convergence from retina to thalamus. Cell *173*, 1343–1355.e24. https://doi.org/10.1016/j.cell.2018.04.

48. Reimer, J., Froudarakis, E., Cadwell, C.R., Yatsenko, D., Denfield, G.H., and Tolias, A.S. (2014). Pupil Fluctuations Track Fast Switching of Cortical States during Quiet Wakefulness. Neuron *84*, 355–362. https://doi.org/10.1016/j.neuron.2014.09.033.

49. Vinck, M., Batista-Brito, R., Knoblich, U., and Cardin, J.A. (2015). Arousal and Locomotion Make Distinct Contributions to Cortical Activity Patterns and Visual Encoding. Neuron *86*, 740–754. https://doi.org/10.1016/j.neuron.2015.03.028.

50. Franke, K., Willeke, K.F., Ponder, K., Galdamez, M., Zhou, N., Muhammad, T., Patel, S., Froudarakis, E., Reimer, J., Sinz, F.H., and Tolias, A. S. (2022). State-dependent pupil dilation rapidly shifts visual feature selectivity. Nature *610*, 128–134.

51. Boissonnet, T., Tripodi, M., and Asari, H. (2023). Awake responses suggest inefficient dense coding in the mouse retina. Elife *12*, e78005. https://doi.org/10.7554/elife.78005.

52. Felsen, G., and Dan, Y. (2005). A natural approach to studying vision. Nat. Neurosci. *8*, 1643–1646. https://doi.org/10.1038/nn1608.

53. Parker, P.R.L., Abe, E.T.T., Leonard, E.S.P., Martins, D.M., and Niell, C. M. (2022). Joint coding of visual input and eye/head position in v1 of freely moving mice. Neuron *110*, 3897–3906.e5. https://doi.org/10.1016/j.neuron.2022.08.029.

54. Harris, K.D. (2020). A shift test for independence in generic time series. Preprint at arXiv. https://doi.org/10.48550/ARXIV.2012.06862.

55. Piscopo, D.M., El-Danaf, R.N., Huberman, A.D., and Niell, C.M. (2013). Diverse Visual Features Encoded in Mouse Lateral Geniculate Nucleus. J. Neurosci. *33*, 4642–4656. https://doi.org/10.1523/JNEUROSCI.5187-12.2013.

56. Durand, S., Iyer, R., Mizuseki, K., De Vries, S., Mihalas, S., and Reid, R.C. (2016). A comparison of visual response properties in the lateral geniculate nucleus and primary visual cortex of awake and anesthetized mice. J. Neurosci. *36*, 12144–12156. https://doi.org/10.1523/JNEUROSCI.1741-16.2016.

57. Tang, J., Ardila Jimenez, S.C., Chakraborty, S., and Schultz, S.R. (2016). Visual receptive field properties of neurons in the mouse lateral geniculate nucleus. PLoS One *11*, e0146017. https://doi.org/10.1371/journal.pone.0146017.

58. Grubb, M.S., and Thompson, I.D. (2003). Quantitative characterization of visual response properties in the mouse dorsal lateral geniculate nucleus. J. Neurophysiol. *90*, 3594–3607. https://doi.org/10.1152/jn.00699.2003.

59. Olshausen, B.A., and Field, D.J. (2005). How close are we to understanding V1? Neural Comput. *17*, 1665–1699.

60. Dearnley, B., Jones, M., Dervinis, M., and Okun, M. (2023). Brain state transitions primarily impact the spontaneous rate of slow-firing neurons. Cell Rep. *42*, 113185. https://doi.org/10.1016/j.celrep.2023.113185.

61. Niell, C.M., and Stryker, M.P. (2010). Modulation of visual responses by behavioral state in mouse visual cortex. Neuron *65*, 472–479.

62. Sillito, A.M., and Jones, H.E. (2002). Corticothalamic interactions in the transfer of visual information. Philos. Trans. R. Soc. Lond. B Biol. Sci. *357*, 1739–1752. https://doi.org/10.1098/rstb.2002.1170.

63. Usrey, W.M., Reppas, J.B., and Reid, R.C. (1998). Paired-spike interactions and synaptic efficacy of retinal inputs to the thalamus. Nature *395*, 384–387. https://doi.org/10.1038/26487.

64. Alonso, J.M., Usrey, W.M., and Reid, R.C. (1996). Precisely correlated firing in cells of the lateral geniculate nucleus. Nature *383*, 815–819. https://doi.org/10.1038/383815a0.

65. Lien, A.D., and Scanziani, M. (2018). Cortical direction selectivity emerges at convergence of thalamic synapses. Nature *558*, 80–86. https://doi.org/10.1038/s41586-018-0148-5.

66. Lesica, N.A., Jin, J., Weng, C., Yeh, C.i., Butts, D.A., Stanley, G.B., and Alonso, J.m. (2007). Adaptation to stimulus contrast and correlations during natural visual stimulation. Neuron *55*, 479–491.

67. Siegle, J.H., Jia, X., Durand, S., Gale, S., Bennett, C., Graddis, N., Heller, G., Ramirez, T.K., Choi, H., Luviano, J.A., et al. (2021). Survey of spiking in the mouse visual system reveals functional hierarchy. Nature *592*, 86–92.

68. Sanzeni, A., Palmigiano, A., Nguyen, T.H., Luo, J., Nassi, J.J., Reynolds, J.H., Histed, M.H., Miller, K.D., and Brunel, N. (2023). Mechanisms underlying reshuffling of visual responses by optogenetic stimulation in mice and monkeys. Neuron *111*, 4102–4115.e9. https://doi.org/10.1016/j.neuron.2023.09.018.

69. Reinhold, K., Resulaj, A., and Scanziani, M. (2023). Brain state-dependent modulation of thalamic visual processing by cortico-thalamic feedback. J. Neurosci. *43*, 1540–1554. https://doi.org/10.1523/jneurosci.2124-21.2022.

70. Kim, J., Matney, C.J., Blankenship, A., Hestrin, S., and Brown, S.P. (2014). Layer 6 corticothalamic neurons activate a cortical output layer, layer 5a. J. Neurosci. *34*, 9656–9664. https://doi.org/10.1523/jneurosci.1325-14.2014.

71. Mante, V., Bonin, V., and Carandini, M. (2008). Functional Mechanisms Shaping Lateral Geniculate Responses to Artificial and Natural Stimuli. Neuron *58*, 625–638. https://doi.org/10.1016/j.neuron.2008.03.011.

72. Coen-Cagli, R., Kohn, A., and Schwartz, O. (2015). Flexible gating of contextual influences in natural vision. Nat. Neurosci. *18*, 1648–1655. https://doi.org/10.1038/nn.4128.

73. Weber, A.I., and Pillow, J.W. (2017). Capturing the dynamical repertoire of single neurons with generalized linear models. Neural Comput. *29*, 3260–3289. https://doi.org/10.1162/neco_a_01021.

74. Sherman, S.M. (2001). Tonic and burst firing: Dual modes of thalamocortical relay. Trends Neurosci. *24*, 122–126. https://doi.org/10.1016/S0166-2236(00)01714-8.

75. Lesica, N.A., Weng, C., Jin, J., Yeh, C.I., Alonso, J.M., and Stanley, G.B. (2006). Dynamic encoding of natural luminance sequences by LGN bursts. PLoS Biol. *4*, e209. https://doi.org/10.1371/journal.pbio.0040209.

76. Mounier, E., Abdullah, B., Mahdi, H., and Eldawlatly, S. (2021). A deep convolutional visual encoding model of neuronal responses in the LGN. Brain Inform. *8*, 11. https://doi.org/10.1186/s40708-021-00132-6.

77. Yamins, D.L.K., and DiCarlo, J.J. (2016). Using goal-driven deep learning models to understand sensory cortex. Nat. Neurosci. *19*, 356–365.

78. Lindsey, J., Ocko, S.A., Ganguli, S., and Deny, S. (2019). A unified theory of early visual representations from retina to cortex through anatomically constrained deep cnns. Preprint at arXiv. https://doi.org/10.48550/arXiv.1901.00945.

79. Doshi-Velez, F., and Kim, B. (2017). Towards a rigorous science of interpretable machine learning. Preprint at arXiv. https://doi.org/10.48550/arXiv.1702.08608.

80. Geirhos, R., Rubisch, P., Michaelis, C., Bethge, M., Wichmann, F.A., and Brendel, W. (2022). Imagenet-trained cnns are biased towards texture; increasing shape bias improves accuracy and robustness. Preprint at arXiv. https://doi.org/10.48550/arXiv.1811.12231.

81. Goldin, M.A., Lefebvre, B., Virgili, S., Pham Van Cang, M.K., Ecker, A., Mora, T., Ferrari, U., and Marre, O. (2022). Context-dependent selectivity to natural images in the retina. Nat. Commun. *13*, 5556.
82. Walker, E.Y., Sinz, F.H., Cobos, E., Muhammad, T., Froudarakis, E., Fahey, P.G., Ecker, A.S., Reimer, J., Pitkow, X., and Tolias, A.S. (2019). Inception loops discover what excites neurons most using deep predictive models. Nat. Neurosci. *22*, 2060–2065. https://doi.org/10.1038/s41593-019-0517-x.
83. Sherman, S.M., and Guillery, R.W. (2002). The role of the thalamus in the flow of information to the cortex. Philos. Trans. R. Soc. Lond. B Biol. Sci. *357*, 1695–1708. https://doi.org/10.1098/rstb.2002.1161.
84. Mineault, P.J., Tring, E., Trachtenberg, J.T., and Ringach, D.L. (2016). Enhanced Spatial Resolution During Locomotion and Heightened Attention in Mouse Primary Visual Cortex. J. Neurosci. *36*, 6382–6392. https://doi.org/10.1523/JNEUROSCI.0430-16.2016.
85. Zhu, S., Hasse, J.m., and Briggs, F. (2021). Optogenetic suppression of corticogeniculate feedback in anesthetized ferrets is overridden by visual stimulation. Preprint at bioRxiv. https://doi.org/10.1101/2021.06.28.450254.
86. Herrero, J.L., Gieselmann, M.A., Sanayei, M., and Thiele, A. (2013). Attention-induced variance and noise correlation reduction in macaque v1 is mediated by nmda receptors. Neuron *78*, 729–739.
87. Thiele, A. (2009). Optimizing brain processing. Nat. Neurosci. *12*, 1359–1360.
88. Roelfsema, P.R., and de Lange, F.P. (2016). Early visual cortex as a multiscale cognitive blackboard. Annu. Rev. Vis. Sci. *2*, 131–151.
89. Lamme, V.A., and Roelfsema, P.R. (2000). The distinct modes of vision offered by feedforward and recurrent processing. Trends Neurosci. *23*, 571–579.
90. Zhang, S., Xu, M., Kamigaki, T., Hoang Do, J.P., Chang, W.C., Jenvay, S., Miyamichi, K., Luo, L., and Dan, Y. (2014). Long-range and local circuits for top-down modulation of visual cortex processing. Science *345*, 660–665. https://doi.org/10.1126/science.1254126.
91. Vinje, W.E., and Gallant, J.L. (2000). Sparse coding and decorrelation in primary visual cortex during natural vision. Science *287*, 1273–1276.
92. Yatsenko, D., Walker, E.Y., and Tolias, A.S. (2018). DataJoint: A simpler relational data model. Preprint at arXiv. https://doi.org/10.48550/arXiv.1807.11104.
93. Pachitariu, M., Steinmetz, N., Kadir, S., Carandini, M., and Kenneth D, H. (2016). Kilosort: realtime spike-sorting for extracellular electrophysiology with hundreds of channels. Preprint at bioRxiv. https://doi.org/10.1101/061481.
94. Spacek, M., Blanche, T., and Swindale, N. (2008). Python for large-scale electrophysiology. Front. Neuroinform. *2*, 9. https://doi.org/10.3389/neuro.11.009.2008.
95. Wietek, J., Rodriguez-Rozada, S., Tutas, J., Tenedini, F., Grimm, C., Oertner, T.G., Soba, P., Hegemann, P., and Wiegert, J.S. (2017). Anion-conducting channelrhodopsins with tuned spectra and modified kinetics engineered for optogenetic manipulation of behavior. Sci. Rep. *7*, 14957–15018. https://doi.org/10.1038/s41598-017-14330-y.
96. Govorunova, E.G., Sineshchekov, O.A., Janz, R., Liu, X., and Spudich, J. L. (2015). Natural light-gated anion channels: A family of microbial rhodopsins for advanced optogenetics. Science *349*, 647–650. https://doi.org/10.1126/science.aaa7484.
97. Madisen, L., Zwingman, T.A., Sunkin, S.M., Oh, S.W., Zariwala, H.A., Gu, H., Ng, L.L., Palmiter, R.D., Hawrylycz, M.J., Jones, A.R., et al. (2010). A robust and highthroughput Cre reporting and characterization system for the whole mouse brain. Nat. Neurosci. *13*, 133–140. https://doi.org/10.1038/nn.2467.A.
98. Huang, Z.J., and Zeng, H. (2013). Genetic approaches to neural circuits in the mouse. Annu. Rev. Neurosci. *36*, 183–215. https://doi.org/10.1146/annurev-neuro-062012-170307.
99. Bortone, D.S., Olsen, S.R., and Scanziani, M. (2014). Translaminar inhibitory cells recruited by layer 6 corticothalamic neurons suppress visual cortex. Neuron *82*, 474–485. https://doi.org/10.1016/j.neuron.2014.02.021.
100. Frandolig, J.E., Matney, C.J., Lee, K., Kim, J., Chevée, M., Kim, S.J., Bickert, A.A., Brown, S.P., and Brown, S.P. (2019). The Synaptic Organization of Layer 6 Circuits Reveals Inhibition as a Major Output of a Neocortical Sublamina. Cell Rep. *28*, 3131–3143.e5. https://doi.org/10.1016/j.celrep.2019.08.048.
101. Mahn, M., Prigge, M., Ron, S., Levy, R., and Yizhar, O. (2016). Biophysical constraints of optogenetic inhibition at presynaptic terminals. Nat. Neurosci. *19*, 554–556. https://doi.org/10.1038/nn.4266.
102. Wiegert, J.S., and Oertner, T.G. (2016). How (not) to silence long-range projections with light. Nat. Neurosci. *19*, 527–528. https://doi.org/10.1038/nn.4270.
103. Wiegert, J.S., Mahn, M., Prigge, M., Printz, Y., and Yizhar, O. (2017). Silencing Neurons: Tools, Applications, and Experimental Constraints. Neuron *95*, 504–529. https://doi.org/10.1016/j.neuron.2017.06.050.
104. Poynton, C.A. (1998). Rehabilitation of gamma. In Human Vision and Electronic Imaging III, *3299*, B.E. Rogowitz and T.N. Pappas, eds. (International Society for Optical Engineering), pp. 232–249. https://doi.org/10.1117/12.320126. http://www.poynton.com/PDFs/Rehabilitation_of_gamma.pdf.
105. Rueden, C.T., Schindelin, J., Hiner, M.C., DeZonia, B.E., Walter, A.E., Arena, E.T., and Eliceiri, K.W. (2017). ImageJ2: ImageJ for the next generation of scientific image data. BMC Bioinf. *18*, 529. https://doi.org/10.1186/s12859-017-1934-z.
106. Schindelin, J., Arganda-Carreras, I., Frise, E., Kaynig, V., Longair, M., Pietzsch, T., Preibisch, S., Rueden, C., Saalfeld, S., Schmid, B., et al. (2012). Fiji: An open-source platform for biological-image analysis. Nat. Methods *9*, 676–682. https://doi.org/10.1038/nmeth.2019.
107. Swindale, N.V., and Spacek, M.A. (2014). Spike sorting for polytrodes: a divide and conquer approach. Front. Syst. Neurosci. *8*, 6. https://doi.org/10.3389/fnsys.2014.00006.
108. Román Rosón, M., Bauer, Y., Kotkat, A.H., Berens, P., Euler, T., and Busse, L. (2019). Mouse dLGN Receives Functional Input from a Diverse Population of Retinal Ganglion Cells with Limited Convergence. Neuron *102*, 462–476. https://doi.org/10.1016/j.neuron.2019.01.040.
109. Goard, M., and Dan, Y. (2009). Basal forebrain activation enhances cortical coding of natural scenes. Nat. Neurosci. *12*, 1444–1449. https://doi.org/10.1038/nn.2402.

STAR★METHODS

KEY RESOURCES TABLE

REAGENT or RESOURCE	SOURCE	IDENTIFIER
Bacterial and virus strains		
Cre-dependent, stGtACR2-expressing adeno-associated virus (pAAV hSyn1-SIO-stGtACR2-FusionRed)	Addgene	RRID:Addgene_105677
Deposited data		
This study		https://doi.org/10.5281/zenodo.15479878
Electrophysiological data	Spacek et al.[10]	https://doi.org/10.12751/g-node.58bc8k
Experimental models: Organisms/strains		
B6.FVB(Cg)-Tg(Ntsr1-cre)GN220Gsat/Mmcd; MMRR	Mutant Mouse Resource and Research Center (MMRRC)	RRID:MMRRC_030648-UCD
Software and algorithms		
This study		https://doi.org/10.5281/zenodo.15058825
Fiji/ImageJ	NIH	https://imagej.net/; RRID: SCR_003070
Datajoint	Yatsenko et al.[92]	https://datajoint.org/; RRID: SCR_014543
RFEst	Huang et al.[39]	https://github.com/berenslab/RFEst
EXPO visual display software	developed by Dr. Peter Lennie and maintained by Rob Dotson for the Center for Neural Science at New York University	
Kilosort & Kilosort2	Pachitariu et al.[93]	https://zenodo.org/records/4482749; RRID:SCR_016422
Spyke	Spacek et al.[94]	https://spyke.github.io/
Other		
Hamilton syringe	Hamilton, Bonaduz, Switzerland	Gastight (10 ml); Model#1701
Stereotactic frame	Neurostar, Tuebingen, DE	Robot Stereotaxic
Closed loop temperature control system for small rodents	WPI Germany, Berlin, Germany	ATC 1000
Sharp micropipette	Science Products, Hofheim, DE	GB150F-8P
Vibratome	Leica, Wetzlar, Germany	Leica VT1200 S
DAPI-containing mounting medium	Thermo Fisher Scientific, Waltham, Massachusetts, USA	Vectashield DAPI
DiI	Invitrogen, Carlsbad, USA	
Olympus BX61 Upright Wide Field Microscope	Olympus, Tokyo, Japan	RRID:SCR_020343
OptiBond FL primer and adhesive	Kerr dental, Rastatt, DE	Cat#35369
Dental cement	Ivoclar Vivadent, Ellwangen, DE	Tetric EvoFlow
Ground and reference screws	Bilaney	00-96 X 1/16 stainless steel screws
Kwik-Cast	WPI Germany, Berlin, DE	https://www.wpi-europe.com/products/laboratory-supplies/adhesives.aspx
Gamma-corrected LCD screen	Samsung	Samsung SyncMaster 2233
32-channel edge silicon probes	Neuronexus, Ann Arbor, USA	A1x32Edge-5mm-20-177-A32
Arduino-type microcontroller	Arduino	http://www.arduino.cc/
Infrared camera (Guppy AVT camera)	Allied Vision, Exton, USA	Guppy AVT camera
Blue light (blue LED, center wavelength 465 nm)	Doric Lenses, Quebec, Canada	LEDC2 465/635 SMA
Optic fiber	Doric Lenses, Quebec, Canada	MFP_480/500/1000-0.63_m_SMA
Blackrock microsystems amplifier	Blackrock Microsystems Europe GmbH, Hannover DE	128-Channel Neural signal processor

EXPERIMENTAL MODEL AND SUBJECT DETAILS

All procedures complied with the European Communities Council Directive 2010/63/EU and the German Law for Protection of Animals, and were approved by local authorities, following appropriate ethics review. Experiments were carried out under License ROB-55.2-2532.Vet_02-17-40 in 4 adult Ntsr1-Cre mice (median age: 15.5 ± 6.45 weeks; B6.FVB(Cg)-Tg(Ntsr1-cre)GN220Gsat/Mmcd; MMRRC) of either sex (1 female, 3 male) and in a male Ntsr1-Cre negative control mouse, in order to assess potential light confounds of the optogenetic manipulations. Prior to experimentation, the genotype of the mice was confirmed via polymerase chain reaction (PCR) analysis. We do not expect that sex plays a role in our study, but future experiments should explicitly address this question.

The mouse strain used for this research project, B6.FVB(Cg)-Tg(Ntsr1-cre)GN220Gsat/Mmucd, RRID:MMRRC_030648-UCD, was obtained from the Mutant Mouse Resource and Research Center (MMRRC) at University of California at Davis, an NIH-funded strain repository, and was donated to the MMRRC by MMRRC at University of California, Davis. Made from the original strain (MMRRC:017266) donated by Nathaniel Heintz, Ph.D., The Rockefeller University, GENSAT and Charles Gerfen, Ph.D., National Institutes of Health, National Institute of Mental Health.

METHOD DETAILS

Surgical procedures

Stereotactic surgeries were performed to implant a head-post for head-fixation, implant a ground/reference screw for electrophysiology, inject a virus for optogenetic feedback manipulation, and drill a craniotomy for acute electrode insertions.

Thirty minutes prior to the surgical procedure, mice were injected with an analgesic (Metamizole, 200 mg/kg, sc, MSD Animal Health, Brussels, Belgium). To induce anesthesia, animals were placed in an induction chamber and exposed to isoflurane (5% in oxygen, CP-Pharma, Burgdorf, Germany). After induction of anesthesia, mice were fixated in a stereotaxic frame (Drill & Microinjection Robot, Neurostar, Tuebingen, Germany) and the isoflurane level was lowered (0.5%–2% in oxygen), such that a stable level of anesthesia could be achieved as judged by the absence of an interstitial reflex. Throughout the procedure, the eyes were covered with an eye ointment (Bepanthen, Bayer, Leverkusen, Germany) and a closed loop temperature control system (ATC 1000, WPI Germany, Berlin, Germany) ensured that the animal's body temperature was maintained at 37°C. At the beginning of the surgical procedure, an additional analgesic was administered (Buprenorphine, 0.1 mg/kg, sc, Bayer, Leverkusen, Germany) and the animal's head was shaved and thoroughly disinfected using iodine solution (Braun, Melsungen, Germany). Before performing a scalp incision along the midline, a local analgesic was delivered (Lidocaine hydrochloride, sc, bela-pharm, Vechta, Germany). The skin covering the skull was partially removed and cleaned from tissue residues with a drop of H_2O_2 (3%, AppliChem, Darmstadt, Germany). Using four reference points (bregma, lambda, and two points 2 mm to the left and to the right of the midline respectively), the animal's head was positioned into a skull-flat configuration for the further steps.

In order to suppress V1 L6 CT feedback selectively and reversibly, we conditionally expressed the chloride-conducting channelrhodopsin stGtACR2[42,95,96] in L6a CT pyramidal cells[5,62,83] by injecting AAV-stGtACR2-RFP into the left hemisphere V1 of Ntsr1-Cre mice[43,97,98] (Figure 1A). Ntsr1+ neurons are known to correspond with >90% specificity to L6 CT pyramidal cells.[6,99,100] Furthermore, the opsin *stGtACR2* restricts expression to somata and the axon-initial segment which prevents possible accidental axonal depolarization due to a differential Cl^- ion reversal potential across different neuronal compartments.[101–103] It also offers improved photocurrents and higher sensitivity, which are of particular relevance to manipulating deeply located L6 CT neurons, while avoiding light artifacts and tissue damage arising from excessive light intensities.[103]

Before surgery, the Cre-dependent, stGtACR2-expressing *adeno-associated virus* (AAV) vector (pAAV_hSyn1-SIO-stGtACR2-FusionRed, Addgene, #105677) stock solution was diluted to 5×10^{11} gc/ml titers, and aliquotted to 4 μl. During surgery, aliquots were front-loaded into a glass pipette mounted on a Hamilton syringe (SYR 10 μl 1701 RN no NDL, Hamilton, Bonaduz, Switzerland), controlled by the Injection Robot of the Neurostar Stereotax. After performing a small craniotomy for injection (100 μm diameter), we injected 300 nl of virus solution into V1 (2×50 nl shots injected at a rate of 50 nl/30 s at a respective depth of 900 μm, 800 μm and 700 μm below the brain surface).

For implant fixation, the exposed skull was covered with OptiBond FL primer and adhesive (Kerr Dental, Rastatt, Germany) omitting three locations: V1 (AP: -3.28 mm, ML: -2.4 mm), dLGN (AP: -2.3 mm, ML: -2 mm), and a position roughly 1.5 mm anterior and 1 mm to the right of bregma, designated for a miniature ground and reference screw. A custom-made lightweight stainless steel head bar was positioned over the posterior part of the skull such that the round opening in the bar was centered on V1/dLGN. The head bar was attached with dental cement (Ivoclar Vivadent, Ellwangen, Germany) to the primer/adhesive. The opening was later filled with the silicone elastomer sealant Kwik-Cast (WPI Germany, Berlin, Germany). Then the miniature screw (00-96 X 1/16 stainless steel screws, Bilaney), which served both as ground and reference that was soldered to a custom-made connector pin, was implanted.

At the end of the procedure, an iodine-based ointment (Braunodivon, 10%, B. Braun, Melsungen, Germany) was applied to the edges of the wound and a long-term analgesic (Meloxicam, 2 mg/kg, sc, Böhringer Ingelheim, Ingelheim, Germany) was administered and for 3 consecutive days. For at least 5 days post-surgery, the animal's health status was assessed via a score sheet. After at least 1 week of recovery, animals were gradually habituated to the experimental setup by first handling them and then simulating the experimental procedure. To allow for virus expression, neural recordings started after an incubation time of 2-4 weeks after injection.

On the day prior to the first day of recording, mice were fully anesthetized using the same procedures as described for the initial surgery, and a craniotomy (ca. 2×1 mm on the AP×BL axes) was performed over dLGN (ca. 2.5 mm posterior from bregma and 2.3 mm lateral from midline) and V1 and re-sealed with Kwik-Cast (WPI Germany, Berlin, Germany). As long as the animals did not show signs of discomfort, the long-term analgesic Metacam was administered only once at the end of surgery, to avoid any confounding effect on experimental results. Recordings were performed daily and continued for as long as the quality of the electrophysiological signals remained high.

Extracellular recordings

After 2-4 weeks of expression time, we performed *in vivo* extracellular multi-electrode array (MEA) recordings of dLGN neurons in awake, head-fixed mice (Figure 1A). Extracellular signals were recorded at 30 kHz (Blackrock microsystems, Blackrock Microsystems Europe GmbH, Hanover, Germany). For each recording session, the silicon plug sealing the craniotomy was removed. For dLGN recordings, a 32-channel linear silicon probe (Neuronexus A1x32Edge-5mm-20-177-A32) was lowered to a depth of $\sim$2500–3500 μm below the brain surface. We judged recording sites to be located in dLGN based on the characteristic progression of RFs from upper to lower visual field along the electrode shank,[55] the presence of responses strongly modulated at the temporal frequency of the drifting gratings (F1 response), and the preference of responses to high temporal frequencies.[55,58] For *post hoc* histological reconstruction of the recording site, the electrode was stained with DiI (Invitrogen, Carlsbad, USA) for some (typically the last) recording sessions.

Locomotion

During the experiment, mice were free to run on an air-floating Styrofoam ball and the run speed was recorded via locomotion sensors (Figure 1A). Two optical computer mice interfaced with a microcontroller (Arduino Duemilanove) sampled ball movements at 90 Hz.

To compute animal run speed, we used the Euclidean norm of three perpendicular components of ball velocity (roll, pitch and yaw) and smoothed traces with a Gaussian kernel (σ = 0.2 s). To quantify the effect of running vs sitting on various response properties, the run modulation index (MI_{Run}) was defined based on the mean firing rates during running vs sitting periods as MI_{Run} = (running - sitting)/(running + sitting), where running periods were defined as those for which speed exceeded 1 cm/s, and sit periods as those for which speed fell below 0.25 cm/s.

To test for a significant difference in mean FRs between the run vs. sit conditions matched for each neuron, we used the Wilcoxon signed-rank test.

Eye tracking

To record eye position and pupil size, the animal's eye that was viewing the stimulus was illuminated with infrared LED light and monitored using a zoom lens (Navitar Zoom 6000) coupled with a camera (Guppy AVT camera; frame rate 50 Hz, Allied Vision, Exton, USA).

Pupil position was extracted from the eye-tracking videos using a custom, semi-automated algorithm. Briefly, each video frame was equalized using an adaptive bi-histogram equalization procedure, and then smoothed using median and bilateral kernels. The center of the pupil was detected by taking the darkest point in a convolution of the kerneled image with a black square. Next, the peaks of the image gradient along lines extending radially from the center point were used to define the pupil contour. Lastly, an ellipse was fit to the contour, and the center and area of this ellipse was taken as the position and size of the pupil, respectively. A similar procedure was used to extract the position of the corneal reflection (CR) of the LED illumination. Eye-closure, grooming, or implausible ellipse fitting was automatically detected and the adjacent data points 0.15 s before and after were excluded. Linear interpolation and a subsequent Gaussian smoothing (σ = 0.06 s) was applied to fill the removed segments. Adjustable algorithm parameters, such as the threshold of the mean pixel-wise difference between each frame and a reference frame to detect blinks, were set manually for each experiment.

To quantify the effect of large vs small pupil sizes on various response properties, the eye modulation index (MI_{Pupil}) was defined based on the mean firing rates during periods of large vs small pupils as MI_{Pupil} = (pupil large - pupil small) / (pupil large + pupil small), where periods of large pupils were defined as those for which pupil size was above the 50th percentile of the median normalized pupil trace, and periods of small pupils as those for which pupil size fell below the 25th percentile.

Optogenetic feedback suppression

To photosuppress V1 Ntsr1+ L6 CT pyramidal cells, an optic fiber (480 μm core diameter, MFP_480/500/1000-0.63_m_SMA, Doric Lenses, Quebec, Canada) was coupled to a light-emitting diode (blue LED, center wavelength 465 nm, LEDC2_465/635_SMA, Doric Lenses, Quebec, Canada) and positioned with a micromanipulator less than 1 mm above the exposed surface of V1. A black metal foil surrounding the tip of the head bar holder prevented the photostimulation light from reaching the animal's eyes. To ensure that the photostimulation was effective, the first recording session for each mouse was carried out in V1. Only if the exposure to light reliably induced suppression of V1 activity was the animal used for subsequent dLGN recordings. LED light intensity was adjusted on a daily basis to evoke reliable effects and account for variations in exact virus titer, volume, incubation time, virus expression levels, and fiber position (0.85-9.5 mW at the fiber tip). Since the tip of the fiber never directly touched the surface of the brain, and since the clarity of the surface of the brain varied (generally decreasing every day following the craniotomy), the light intensity delivered even to superficial layers of V1 was inevitably lower. For the movie stimulus, optogenetic pulses of 1 s duration were sent randomly each second with a 50% chance.

To quantify the effect of CT feedback suppression on various response properties, we defined the optogenetic modulation index ($MI_{\text{CT FB supp}}$) based on the mean FRs during CT feedback suppression ('opto') versus the control condition as $MI_{\text{CT FB supp}}$ = (opto - control)/(opto + control). To quantify the temporal dynamics of the effect of suppressing CT feedback with optogenetic pulses, we calculated rate of change (RoC) in the neurons' responses based on both data and model prediction (see below). For each case, we first identified the time point t_min where the slope of neurons response flipped its sign. Then, we calculated the normalised change in responses $MI_{\text{CT FB supp}}$ Finally, *RoC* was defined as: $RoC = MI_{\text{CT FB supp}}/t_{\text{min}}$.

Joint modulation by additional inputs

In order to quantify the joint effect of all the modulatory inputs, we calculated MI_{Joint} as

$$MI_{\text{Joint}} = 1 - \left(1 - MI_{\text{CT FB supp}}\right)\left(1 - MI_{\text{Run}}\right)\left(1 - MI_{\text{Pupil}}\right)$$

To test for the correlations between the variables of interest *stimulus, opto, run, and eye*, we computed their cross-correlations for all time points for which we had valid data (e.g. removing periods with eye blinks). We then used the delay time to shift the traces appropriately before computing their correlation value (Pearson's r; Figure S3C). To test for significance while accounting for auto-correlations we used a permutation test.[54]

Visual stimulation

During the experiment, the mice were passively viewing visual stimuli on an LCD monitor screen in their right visual field. The visual stimuli were presented on a gamma-calibrated liquid crystal display (LCD) monitor (Samsung SyncMaster 2233RZ, 47×29 cm, 1680×1050 resolution at 60 Hz, mean luminance 50 cd/m^2) positioned at a distance of 25 cm from the animal's right eye (spanning ~108×66° visual angle by small angle approximation) using custom written software (EXPO, https://sites.google.com/a/nyu.edu/expo/home). The display was gamma-corrected for the presentation of artificial stimuli, but not for movies (see below).

For movie stimulus generation, we adopted a set of randomly picked clips from various movies. Briefly, source movie clips were converted to grey scale, temporally downsampled to 30 frames per s, spatially resampled and cropped to 424×264 pixels, to be presented on our 47×29 cm monitor screen at 25 cm distance at 106×66° (4 pixels/°) visual angle (by small angle approximation, which preserves the desired pixel resolution at the screen center better than the arctangent). Movie frames were not histogram-equalized and presented at 60 Hz (repeating each frame twice) without monitor gamma correction, since cameras are already gamma corrected for consumer displays.[104] To generate the movie sequence, we used a random set of 296 unique movie clips (5 s each) and split 188/296 clips into 8 parts of 36 unique clips (5 s×36 = 180 s per part). They were interleaved with set of 8 clips (5 s×8 = 40 s) which was repeated 9 times. The repeated clips served to give an estimate of response reliability to the same clips. The movie sequence was flanked by a period of blank grey screen presentation (1 min) at the beginning and at the end, to record spontaneous activity. This resulted in a total stimulus duration of ~32 mins. To rule out sequence effects, we randomized the clip order for different stimulus presentations. To investigate the effects of L6 CT FB suppression, we simultaneously presented a random optogenetic pulse train of 1 s pulses, occurring each second with a probability of 50%, throughout the entire stimulus duration, including blank grey screen periods.

To measure RFs in a more standard manner, we also presented an (artificial) sparse noise stimulus. The stimulus consisted of a rapid sequence of non-overlapping white and black squares appearing in succession within a 12x12 square grid presented on a grey background of mean luminance (50 cd/m^2). The square grid spanned 60° per side, while individual squares spanned 5° per side. Each square flashed 20 times for 200 ms at random order. The stimulus triggered average (STA) for the sparse noise stimulus was computed using the onset of each square and then computing the normalised mean spike rate triggered by each position.

To categorize neurons into functional subtypes (see below), we used a full-field light intensity step stimulus. The stimulus consisted of four sequential light intensity levels, each presented for two seconds: a dark level (0% intensity), a bright level (100% intensity), a return to the dark level (0% intensity), and a medium level (50% intensity).

Histology

To verify virus expression and recording sites, we performed post-mortem histological analyses. After the final recording session, mice were first administered an analgesic (Metamizole, 200 mg/kg, sc, MSD Animal Health, Brussels, Belgium) and following a 30 min latency period were transcardially perfused under deep anesthesia using a cocktail of Medetomidin (Domitor, 0.5 mg/kg, Vetoquinol, Ismaning, Germany), Midazolam (Climasol, 5 mg/kg, Ratiopharm, Ulm, Germany) and Fentanyl (Fentadon, 0.05 mg/kg, Dechra Veterinary Products Deutschland, Aulendorf, Germany) (ip). Perfusion was first done with Ringer's lactate solution followed by 4% paraformaldehyde (PFA) in 0.2 M sodium phosphate buffer (PBS). Brains were removed, postfixed in PFA for 24 h, and then rinsed with and stored in PBS at 4°C. Slices (50 μm) were cut using a vibrotome (Leica VT1200 S, Leica, Wetzlar, Germany), stained with DAPI-solution (DAPI, Thermo Fisher Scientific, Waltham, Massachusetts, USA), mounted on glass slides with Vectashield mounting medium (Vectashield H-1000, Vector Laboratories, Burlingame, USA), and coverslipped. A scanning fluorescent microscope (BX61, Olympus, Tokyo, Japan) was used to inspect slices for the presence of red fluorescent protein (RFP/FusionRed) marking stGtACR2-channels, and DiI, marking electrode tracks. Recorded images were processed off-line using FIJI.[105,106]

QUANTIFICATION AND STATISTICAL ANALYSIS

Spike sorting and unit extraction

Spike sorting was performed to obtain single unit activity from extracellular recordings. Electrophysiological signal recordings were filtered using a 4th-order Butterworth high-pass non-causal kernel with a low frequency cutoff of 300 Hz. We then used the open source, MATLAB-based (The Mathworks, Natick, Massachusetts, USA), automated spike sorting toolbox Kilosort and Kilosort2.[93] Resulting clusters were manually refined using Spyke,[94] a Python application that allows for the selection of channels and time ranges around clustered spikes for realignment, as well as representation in 3D space using dimension reduction (multichannel PCA, ICA, and/or spike time). In 3D, clusters were then further split via a gradient-ascent based clustering algorithm (GAC).[107] Exhaustive pairwise comparisons of similar clusters allowed the merger of potentially over-clustered units. For subsequent analyses, we inspected autocorrelograms and mean voltage traces, and only considered units that displayed a clear refractory period and a distinct spike waveshape.

Unit quality metrics

To evaluate the quality of the sorted units, we performed a *post-hoc* analysis using several quality metrics.

1. Signal-to-noise ratio (SNR; Figure S10A). For each neuron, we assessed the SNR as: $SNR = A_s/\sigma_n$, where A_s is the maximum amplitude of the mean spike waveform on the best channel, and σ_n is the background noise level on the best channel calculated as the median absolute deviation.
2. Interspike interval (ISI) violations (Figure S10B). For each neuron, we calculated the percentage of spikes violating an ISI of 1.5 ms.
3. Isolation distance (Figures S10C–S10G). We randomly sampled 1000 spikes from each extracted unit and conducted pairwise comparisons between simultaneously recorded pairs of units. Waveforms recorded across all channels were projected into a lower-dimensional space using the first three principal components (PCA; Figure S10C). We then calculated the within-cluster distance as the average Euclidean distance between spikes belonging to the same cluster and the minimum isolation distance as the smallest average distance to spikes from any other cluster recorded in the same session (Figure S10D). Additionally, we computed the cluster centres in PCA space and projected spikes onto the line connecting the centres of any two clusters (Figure S10E). This projection allowed us to calculate the discriminability of neurons using the *d*-prime measure (Figure S10F). Finally, we utilized *NDsep* (Figure S10H), a preferred metric of cluster separation employed by Spyke,[94,107] as it avoids the loss of information associated with projecting 3D clusters onto a single dimension. The *NDsep* for any pair of neurons *i*, *j* was calculated as follows:

$$N = 1 - \frac{1 - \frac{N_{nn}}{N_i}}{1 - \frac{N_i}{N_i + N_j}}, N_i < N_j$$

where N_{nni} is the number of points in cluster *i* whose nearest neighbour is also in cluster *i*. The value ranges from 1 for completely separate clusters, to 0 for completely mixed clusters.[94,107]

Neuronal data analysis

Data analysis was performed using the DataJoint framework[92] with custom-written code in Python. We also used a customized version of RFEst (https://github.com/berenslab/RFEst) to allow for multiple model inputs. To obtain units firing rates in spikes per second (Hz), each unit's spike density function (SDF) was calculated by binning spikes into a firing rate histogram (bin width = 20 ms) and convolving this with a Gaussian of width $2\sigma = 10$ ms. Mean firing rates (FRs) over a given condition were calculated as the mean of the time-varying firing rates for the defined periods. Neurons with mean evoked firing rates < 0.1 Hz were excluded from all further analysis. To compute how reliable a neuron responded to the visual stimulus we used the set of 8 clips that where repeated 9 times throughout the experiment. We computed reliability by correlating each repetition with the mean of all other repetitions and averaging that over all splits.

Reliability of CT feedback suppression

To compute the reliability of the optogenetic manipulation of L6 CT neurons, we developed a trial-based permutation test. In response to drifting gratings, we calculated the average firing rate during each trial and separated the trial with optogenetic CT feedback suppression ($trials_{CT\ FB\ supp}$; n=90-130) from those without ($trials_{control}$; n = 90-130). We calculated the observed statistics $effect_{CT\ FB\ supp}$ as the difference in the means between the $trials_{CT\ FB\ supp}$ and the $trials_{control}$. We assessed significance by permuting trial labels 1000 times and considered the effect significant if it fell outside of the distribution of permuted $effect_{CT\ FB\ supp}$. Finally, we compared the percentage of neurons that passes the significance test between the included recording and a recording from a control mouse (Ntsr-negative).

Spline-based generalized linear model

To estimate the spatio-temporal RFs (stRFs), we used the RFEst Python toolbox for spline-based spatio-temporal RF estimation.[39] By using natural cubic splines as the basis (e.g., Figures S6A–S6D), the estimates are automatically smooth, which is a desirable property for single stRFs. To impose sparsity on the weights we added L1 regularization, which pushed the weights for less relevant bases to zero. To compute the spline-based stRFs, w_{SPL}, the coefficients, b_{SPL}, were obtained as

$$b_{SPL} = \left(S^T X^T X S\right)^{-1} S^T X^T y$$

with X as the stimulus design matrix, y as the neural response vector, and S as the spline matrix. The stRF was computed as

$$w_{SPL} = S b_{SPL} = S\left(S^T X^T X S\right)^{-1} S^T X^T y$$

To approximate w_{SPL} we used a generalized linear model (GLM) that predicts the instantaneous firing rate for one neuron using the movie as a predictor. We extended this "Stimulus only" model by integrating also running speed and pupil size as behavioural predictors of neuronal firing rate. To estimate the effect of cortico-thalamic (CT) feedback, an additional bimodal input was used comprising the optogenetic light stimulation that could be either on (o_t=1) or off (o_t=0). All inputs where parameterized with a set of spline basis and multiplied with an extra weight vector (also referred to as kernel):

$$f(s,o,r,e) = g\left(w_s^T s[t:t-\Delta t] + w_o^T o[t:t-\Delta t] + w_r^T r[t:t-\Delta t] + w_e^T e[t:t-\Delta t]\right)$$

with s, o, r, and e denoting the additional model inputs of stimulus, optogenetics, running and eye, respectively, and $[t:t\text{-}\Delta t]$ defining the temporal integration window (250 ms for stimulus and 800 ms for the predictors for modulatory inputs).

We trained and evaluated the spline-GLM on the recorded dataset as follows: Given the known diversity of mouse dLGN feature selectivity,[55,108] we performed a separate hyperparameter search for each neuron. All GLM fits in this study were cross-validated. The models analysed here were configured with the selected optimal hyperparameters and the reported performance is based on the held-out test set. Specifically, we estimated the kernels by gradient descent with respect to the cost function with L1 regularization. As standard procedure for time series data, we used 150 out of the 188 unique movie clips (80%) for cross-validation to select optimal hyperparameters and reserved the remaining 38 clips (20%) as a held-out test set. To select optimal hyperparameters, we used five-fold cross-validation grid search on the training data (120 training clips and 30 validation clips in each fold). Hyperparameters included the number of spline basis (between 10 and 19) in the temporal dimension (for stimulus, pupil size, locomotion, and feedback input) and spatial dimension (only stimulus), as well as the strength of the L1 regularization (with weights varying from 5 to 15). The stRFs were initialized randomly and optimized using gradient decent for 2000 iterations. We stopped the fitting early when the training cost changed less than 10^{-5} for 10 iterations. Finally, we selected the hyperparameters based on the mean performance on the validation set across folds. After optimal hyperparameter selection, models were retrained on the full training data (150 movie clips) and the final performance of the model was reported as the correlation coefficient between predicted and observed neural responses on the held-out test data (38 movie clips).

We further fitted spline GLMs with responses to a sparse noise stimulus. We conducted a separate hyperparameter search for this stimulus, using a similar procedure as for the movie stimulus, involving cross-validation. For each neuron, we determined a unique set of optimal hyperparameters and kernels for the sparse noise stimulus and the movie stimulus.

Following Harris (2020),[54] we performed a permutation test to evaluate the significance of the model predictors. To achieve this, we provided the model with input data from the validation set of an unrelated session (for the model inputs ‘stimulus’, ‘running’, ‘pupil size’) or with synthetic inputs generated with the same statistics as the original (for the ‘CT feedback suppression’ input), one at a time. We repeated the process using all different data from all recording sessions. Subsequently, we compared for each input the actual model performance (Pearson’s r) on the validation set across its folds (n = 5) against a distribution of model performances with that specific input permuted from the different recording sessions across their folds (n = 5 folds × 9 recording sessions). Inputs were considered significant if the actual performance differed from the permuted performance with $p \leq 0.05$ using the non-paired Mann-Whitney-U test.

Spatio-temporal RF characterization

To separate spatial and temporal components of the 3D stRFs, we performed singular value decomposition (SVD) on the norm of the stimulus weight vector w. The temporal RF was extracted as the first left-singular vector of U, i.e. temporal dimension with the highest variance, and the spatial RF as the first right-singular vector of V, reshaped into the height- and width-dimensions of the input vector w. The extremes of the reshaped spatial RF vector were then used to quantify RF position and RF area. The extracted temporal RF components were normalized and multiplied with the RF center value before computing the slope (-150 ms to peak).

Model spatial RFs were estimated by extracting the 2D spatial RF component from the model weights and then drawing a contour line around the largest absolute peak (assumed to be the center of the spatial RF). The contour threshold was gradually lowered until any further decrease would result in a second contour around the second largest extremum (background irregularities considered as noise). To avoid overly large RFs in very clean spatial components (without any major second extremum), the contour threshold had to be 2 standard deviations above or below the mean. To improve estimate accuracy, the spatial RF component was upsampled 16-fold via cubic spline interpolation. The spatial RF area was estimated by calculating the number of pixels of the spatial RF contour mask and converting it to squared degrees of visual angle.

To quantify the degree of center-surround organisation, similar to Lesica et al. (2007),[66] stRFs were collapsed across the azimuth axis, and accordingly defined as a function of elevation and time. Then, we identified the time point with peak activity. Subsequently, centre regions were defined according to the spatial width of the peak activity, and surround regions were defined as a ring encircling the centre and extending up to twice the diameter or 9∘. We then summed pixel intensities within the centre region and the surround regions separately and calculated surround-to-centre ratio as:

$$\frac{2 \times \sum centre}{\sum surround_1 + \sum surround_2}$$

Cell types clustering

To categorize neurons into functional subtypes, we employed dimensionality reduction (PCA) on their PSTH responses to a full-field light intensity step stimulus. Subsequently, we conducted clustering using a Gaussian mixture model on the principal components, resulting in the identification of four primary groups (Sustained ON, Sustained OFF, Transient, and Mixed). Nevertheless, we observed substantial response diversity even within these main groups. To address this, we further subdivided neurons within each group through empirical selection of cluster numbers, aiming to optimize silhouette scores and reduce the standard error of the PSTH mean response within the subclasses. This two-step clustering approach allowed capturing finer distinctions of response patterns (Figures S5A and S5B).

In order to identify putative excitatory and inhibitory neurons in dLGN, we analysed the extracellular spike waveform. For each neuron, the mean waveform of the maximally responsive electrode channel was obtained, and we used parameters proposed by Molnar et al. (2021).[14] The time between trough and peak (trough-to-peak time) and the height ratio of the peak to the trough were calculated and clustered for a large pool of previously recorded dLGN neurons ($n = 666$). We identified 0.25 ms as a threshold for separating broad spiking, putative relay cells, from narrow spiking, putative local dLGN inhibitory neurons (Figures S6Q–S6T).

Decoding analysis

For our *in silico* experiments to isolate the effects of CT feedback suppression, we used a two-alternative forced choice (2AFC) decoder[31] to analyse if stimulus discriminability was easier with or without feedback. Given two spike trains $\{s_A, s_B\}$ in response to two movie clips $\{A, B\}$ we computed the model log-likelihood for the correct $((s_A, A), (s_B, B))$ and the incorrect pairing $((s_A, B)$, $(s_B, A))$. We used the 'Full model' to predict spike trains in the two feedback conditions, (1) with the CT feedback component intact and (2) with the feedback component suppressed. In both conditions, we used 100 randomly selected 50 ms movie fragments from the test set that had not been used for model fitting and their corresponding responses. Using all possible pairs, we computed the model log-likelihood for the correct and the incorrect pairing in both feedback conditions.[30] The log probability for the correct pairing of response s_A and stimulus A is defined as follows:

$$\log p(s_A|A) = \sum_t s_{A,t} \, log \, \lambda_t(A_t) - \lambda(A_t)$$

where λ is the instantaneous firing rate at time t predicted by the model. Analogously, we computed $\log p(s_B|B)$, $\log p(s_A|B)$, and $\log p(s_B|A)$. A correct choice was made if $\log p(s_A|A) > \log p(s_A|B)$ or $\log p(s_B|B) > \log p(s_B|A)$ respectively. We used the percentage correct over all possible pairs to quantify decoding performance. Finally, we computed the ratio of percentage correct for the CT feedback suppressed condition and the control condition. A ratio > 1 indicates better decoding performance in the feedback suppressed condition and a ratio < 1 in the control condition.

To test the predictions of our *in silico* experiment for *in vivo* data, we analysed dLGN responses to a repeated 5-second natural movie under feedback-suppressed and control conditions (200 trials each) obtained from a published dataset.[10] The decoding analysis employed support vector machines (SVMs) with the following protocol: The data was split into training (160 trials) and test sets (40 trials), and segmented into non-overlapping 50 ms or 500 ms fragments. For computational efficiency, 200 stimulus-response pairs (movie fragment A vs B) were randomly sampled, and SVMs were trained separately for each stimulus pair and condition, with hyperparameters (regularization parameter and RBF kernel coefficient) optimized through 5-fold cross-validation. Performance was evaluated on the held-out test set. For a robust comparison to our dataset, neurons with a positive average effect of CT feedback suppression were excluded. Results for each SVM were considered valid only if the firing rates of at least one of the two response fragments exceeded 5 Hz, and only neurons with at least 10 valid fragment pairs in either the CT feedback suppressed or control condition were included in the final analysis. This selection process resulted in the inclusion of 78 neurons (55% of all neurons).

The fold change (*FC*) was calculated as:

$$FC = log^2\left(M_{CT\ FB\ sup} \ / M_{control}\right)$$

with M representing either decoder accuracy or response reliability.

As in the original publication,[10] response reliability was quantified according to Goard and Dan (2009)[109] as the mean pairwise correlation of all trial pairs of a unit's single-trial responses. Single-trial responses were computed by counting spikes in 20 ms, overlapping time bins at 1 ms resolution. Pearson's correlation was calculated between all possible pairs of trials and then averaged across trials per condition.